



AFRL-AFOSR-VA-TR-2021-0087

Soft Materials for Flexible, Stretchable Hybrid Electronics

**Marks, Tobin
NORTHWESTERN UNIVERSITY
633 CLARK
EVANSTON, IL, 60208
USA**

**08/02/2021
Final Technical Report**

DISTRIBUTION A: Distribution approved for public release.

Air Force Research Laboratory
Air Force Office of Scientific Research
Arlington, Virginia 22203
Air Force Materiel Command

REPORT DOCUMENTATION PAGE

Form Approved
OMB No. 0704-0188

The public reporting burden for this collection of information is estimated to average 1 hour per response, including the time for reviewing instructions, searching existing data sources, gathering and maintaining the data needed, and completing and reviewing the collection of information. Send comments regarding this burden estimate or any other aspect of this collection of information, including suggestions for reducing the burden, to Department of Defense, Washington Headquarters Services, Directorate for Information Operations and Reports (0704-0188), 1215 Jefferson Davis Highway, Suite 1204, Arlington, VA 22202-4302. Respondents should be aware that notwithstanding any other provision of law, no person shall be subject to any penalty for failing to comply with a collection of information if it does not display a currently valid OMB control number.
PLEASE DO NOT RETURN YOUR FORM TO THE ABOVE ADDRESS.

1. REPORT DATE (DD-MM-YYYY) 02-08-2021	2. REPORT TYPE Final	3. DATES COVERED (From - To) 01 May 2018 - 30 Apr 2021
--	--------------------------------	--

4. TITLE AND SUBTITLE Soft Materials for Flexible, Stretchable Hybrid Electronics	5a. CONTRACT NUMBER
	5b. GRANT NUMBER FA9550-18-1-0320
	5c. PROGRAM ELEMENT NUMBER 61102F

6. AUTHOR(S) Tobin Marks	5d. PROJECT NUMBER
	5e. TASK NUMBER
	5f. WORK UNIT NUMBER

7. PERFORMING ORGANIZATION NAME(S) AND ADDRESS(ES) NORTHWESTERN UNIVERSITY 633 CLARK EVANSTON, IL 60208 USA	8. PERFORMING ORGANIZATION REPORT NUMBER
--	---

9. SPONSORING/MONITORING AGENCY NAME(S) AND ADDRESS(ES) AF Office of Scientific Research 875 N. Randolph St. Room 3112 Arlington, VA 22203	10. SPONSOR/MONITOR'S ACRONYM(S) AFRL/AFOSR RTB2
	11. SPONSOR/MONITOR'S REPORT NUMBER(S) AFRL-AFOSR-VA-TR-2021-0087

12. DISTRIBUTION/AVAILABILITY STATEMENT
A Distribution Unlimited: PB Public Release

13. SUPPLEMENTARY NOTES

14. ABSTRACT
Printed electronics based on mechanically agile thin-film transistors (TFTs) and circuitry is a revolutionary new technology of great DoD relevance for fabricating unconventional optoelectronics using high-throughput, inexpensive solution processing/printing on flexible/stretchable substrates. The enabling materials objectives are to understand/implement the science underlying the design of: 1) flexible/stretchable printable semiconductors, dielectrics, and contacts; 2) mechanically flexible, stretchable, lightweight circuits for displays, sensors, medical diagnostics, and energy harvesting/storage, integrated with inexpensive plastics and textiles; 3) bio-electronics with soft/biocompatible/bio-degradable circuitry for tissues and organs. Combining these new materials will yield key circuit elements such as resistors, transistors, capacitors, and combinations thereof, where new functionalities will require mechanical agility, bio-compatibility, and electronics on unconventional substrates, and new processing methodologies for device fabrication. This project, supported by AFOSR, focused on the design and realization of new solution-processable, printable, electronic and passive materials, and to integrate them into flexible and stretchable electronics. The objectives were pursued through the three interconnected tasks. Task 1. Active/Passive Materials. Here we designed, synthesized, characterized, and implemented semiconductors, dielectrics, and conductors which are solution-processable at low temperatures using solvents compatible with "soft" substrates. Objectives: i) Printed p-/n-type TFTs with mobilities > 10 cm²/Vs; ii) Operating voltages < 5 V; iii) Maximum processing temperature = 200 °C. Task 2. Materials Integration on Soft Substrates. Once acceptable TFT solution processability and charge transport metrics were achieved, the next task was integration into building block circuits on substrates such as elastomers, sacrificial transfer films, and tissues. Objectives: i) Printed p-/n-type TFT mobilities > 5 cm²/Vs, operating voltages < 5 V; ii) Prototype circuits such as inverters, ring oscillators, rectifiers, D flip-flops, on soft substrates (thickness < 1µm); iii) Fundamentally understand stretchability and interfacial adhesion effects on TFT/circuit components and soft substrates; iv) Young's modulus < 1GPa, strain-to-break > 5%. Task 3. Stretchable Device Fabrication. Here we worked on the fabrication demonstrator devices on printed/stretchable circuit platforms, including those for displays, sensors, e-tags, and e-skins. Specifically, we focused on fabrication on stretchable plastic foils and, for ultimate applications, tissues using printing techniques. Objectives: i) Complex circuits such comparators, modulators, amplifiers; ii) Flexible devices such as displays and sensors; iii) Understand how performance is affected upon circuit transfer; iv) Understand how environment and mechanical stress affect device performance. The products of Tasks 1-3 were envisioned to be a versatile set of innovative electronic and passive materials as well as processes for manipulating them, enabling fabrication of ultra-flexible/bio-inferable DoD-relevant electronic devices. Furthermore, this study focused on enhancing the understanding of the electronic structure, morphology, and charge transport mechanisms in these unconventional electronic materials and how mechanical stress affects their performance in printed prototype devices.

15. SUBJECT TERMS

16. SECURITY CLASSIFICATION OF:			17. LIMITATION OF ABSTRACT	18. NUMBER OF PAGES	19a. NAME OF RESPONSIBLE PERSON
a. REPORT	b. ABSTRACT	c. THIS PAGE			KENNETH CASTER
U	U	U	UU	40	19b. TELEPHONE NUMBER (Include area code) 0000 0000

Standard Form 298 (Rev.8/98)
Prescribed by ANSI Std. Z39.18

SOFT MATERIALS FOR FLEXIBLE, STRETCHABLE HYBRID ELECTRONICS

July 26, 2021

Tobin J. Marks and Antonio Facchetti, Northwestern University

t-marks@northwestern.edu, a-facchetti@northwestern.edu

Abstract

Printed electronics based on mechanically agile thin-film transistors (TFTs) and circuitry is a revolutionary new technology of great DoD relevance for fabricating unconventional optoelectronics using high-throughput, inexpensive solution processing/printing on flexible/stretchable substrates. The enabling materials objectives are to understand/implement the science underlying the design of: 1) flexible/stretchable printable semiconductors, dielectrics, and contacts; 2) mechanically flexible, stretchable, lightweight circuits for displays, sensors, medical diagnostics, and energy harvesting/storage, integrated with inexpensive plastics and textiles; 3) bio-electronics with soft/biocompatible/bio-degradable circuitry for tissues and organs. Combining these new materials will yield key circuit elements such as resistors, transistors, capacitors, and combinations thereof, where new functionalities will require mechanical agility, bio-compatibility, and electronics on unconventional substrates, and new processing methodologies for device fabrication. This project, supported by AFOSR, focused on the design and realization of new solution-processable, printable, electronic and passive materials, and to integrate them into flexible and stretchable electronics. The objectives were pursued through the three interconnected tasks. Task 1. Active/Passive Materials. Here we designed, synthesized, characterized, and implemented semiconductors, dielectrics, and conductors which are solution-processable at low temperatures using solvents compatible with “soft” substrates. Objectives: *i*) Printed p-/n-type TFTs with mobilities $> 10 \text{ cm}^2/\text{Vs}$; *ii*) Operating voltages $\leq 5 \text{ V}$; *iii*) Maximum processing temperature = $200 \text{ }^\circ\text{C}$. Task 2. Materials Integration on Soft Substrates. Once acceptable TFT solution processability and charge transport metrics were achieved, the next task was integration into building block circuits on substrates such as elastomers, sacrificial transfer films, and tissues. Objectives: *i*) Printed p-/n-type TFT mobilities $> 5 \text{ cm}^2/\text{Vs}$, operating voltages $< 5 \text{ V}$; *ii*) Prototype circuits such as inverters, ring oscillators, rectifiers, D flip-flops, on soft substrates (thickness $< 1 \mu\text{m}$); *iii*) Fundamentally understand stretchability and interfacial adhesion effects on TFT/circuit components and soft substrates; *iv*) Young’s modulus $< 1 \text{ GPa}$, strain-to-break $> 5\%$. Task 3. Stretchable Device Fabrication. Here we worked on the fabrication demonstrator devices on printed/stretchable circuit platforms, including those for displays, sensors, e-tags, and e-skins. Specifically, we focused on fabrication on stretchable plastic foils and, for ultimate applications, tissues using printing techniques. Objectives: *i*) Complex circuits such comparators, modulators, amplifiers; *ii*) Flexible devices such as displays and sensors; *iii*) Understand how performance is affected upon circuit transfer; *iv*) Understand how environment and mechanical stress affect device performance.

The products of Tasks 1-3 were envisioned to be a versatile set of innovative electronic and passive materials as well as processes for manipulating them, enabling fabrication of ultraflexible/bio-integrable DoD-relevant electronic devices. Furthermore, this study focused on enhancing the understanding of the electronic structure, morphology, and charge transport mechanisms in these unconventional electronic materials and how mechanical stress affects their performance in printed prototype devices.

Report Details

This document summarizes results from our efforts to develop new flexible and stretchable optoelectronic materials and devices compatible with textile and skin functions/operations following our proposal's outlines. Particularly we emphasized activities focused on identifying new materials with enhanced figures-of-merit in combination with greater intrinsic flexibility/stretchability and processability from solution also using environmentally friendly solvents. Furthermore, we report on new unconventional (vertical) device architecture achieving figure of merits unreported to date.

Synthesis of Polymeric and Molecular Semiconductors

One of the major tasks of this project has been to design, synthesize, and characterize new π -conjugated building blocks for the realization of both n- (electron- transporting) and p-type (hole transporting) polymer semiconductors having greater mechanical stress tolerance. This included addressing the issue of the passivation of grain boundaries of molecular semiconductors, to enhance plasticity, using newly realized semiconducting polymer binders. Finally, we also developed strategies to synthesize and process organic semiconductors using more sustainable, and “greener” synthetic and processing approaches. The results below, only partially published, demonstrate we have made considerable progress on this front.

N-type Polymers and Small Molecules. The electron-transporting properties of n-type polymers, needed for complementary circuits, strongly depend on the chemical and electronic structure of the electron-deficient building blocks. Here we design and developed a novel electron-deficient unit, a thienopyridine fused naphthalene amide (TPNA), via π -conjugative extension at the diagonal position of the widely investigated naphthalene diimide (NDI) moiety, to address the severe π -backbone twisting of typical NDI-based polymers (**Figure 1**).

This strategy should also rigidify the polymer backbone, enhancing intramolecular charge transport. The TPNA-based homopolymer (Homo-TPNA), donor-acceptor copolymer (TPNA-T, T = thienyl), and all-acceptor copolymer (TPNA-BTz, BTz = benzothiadiazole) were synthesized and characterized. Compared to the classical NDI unit of widely investigated poly{[N,N'-bis(2-octyldodecyl)naphthalene-1,4,5,8-

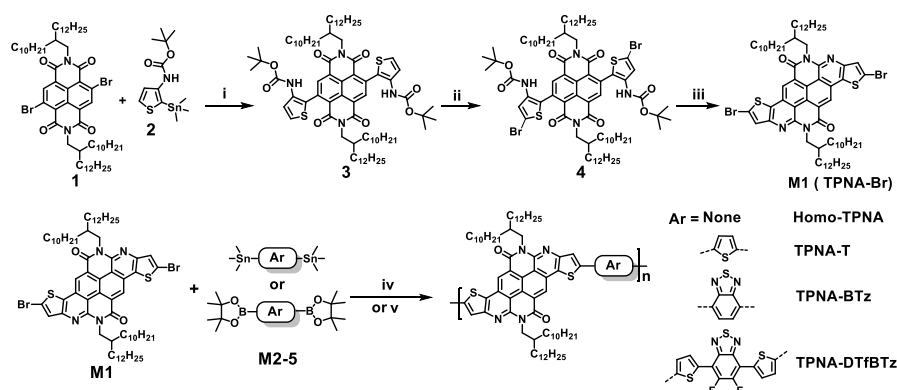


Figure 1. Synthetic route to the monomer TPNA-Br (**M1**) and corresponding polymers. Conditions: (i) Pd(PPh₃)₄, toluene, 110 °C; (ii) NBS, chloroform/DMF, RT; (iii) Trifluoroacetic acid, anisole, DCM, reflux overnight; then triethylamine, 80 °C, overnight; (iv) Pd₂(dba)₃, P(o-tol)₃, CuI, toluene, 150 °C (for **Homo-TPNA**, **TPNA-T**, and **TPNA-DTfBTz**); (v) Pd₂(dba)₃, P(o-tol)₃, K₃PO₄, methyl trioctyl ammonium chloride, toluene/H₂O, 100 °C (for **TPNA-BTz**).

bis(dicarboximide)-2,6-diyl]-alt-5,5'-(2,2'-bithiophene)} (**N2200**) first developed by our group in 2009, TPNA promotes greater π -conjugation, increased electron delocalization, and a nearly planar backbone conformation due to the reduced steric demands of the TPNA-aryl connecting points. 2D GIWAXS indicates that all the TPNA-based polymers are significantly crystalline and exhibit well-ordered microstructures with distinctive lamellar diffractions ($h00$) in the out-of-plane direction and close π - π stacking distances of 3.5 ~ 3.6 Å (**Figure 2**). Benefiting from this homopolymer and all-acceptor molecular design strategy, the Homo-TPNA and TPNA-BTz polymers exhibit lower frontier MO energy levels than

TPNA-T, which promote electron injection while blocking hole accumulation.

Thin-film transistors (TFTs) based on the TPNA polymers exhibit n-channel performance with an optimal electron mobility approaching $0.2 \text{ cm}^2 \text{ V}^{-1} \text{ s}^{-1}$ achieved for TPNA-BTz. These results demonstrate that TPNA is an effective building block for constructing n-type polymers with good backbone planarity and promising electron transport properties.

See: Chen, J.; Zhuang, X.; Huang, W.; Su, M.; Feng, L.; Swick, S.; Wang, G.; Chen, Y.; Yu, J.; Guo, X.; Marks, T.J.; Facchetti, A.; π -Extended Naphthalene Diimide Derivatives for N-type Semiconducting Polymers, *Chem. Mater.* **2020**, 32 5317-5326. DOI: 10.1021/acs.chemmater.0c01397.

As noted above, N2200 remains a workhorse for n-type materials for numerous applications including organic field-effect transistors (OFETs), all-polymer solar cells (APSCs) and energy storage devices. However, the large backbone torsion between naphthalenedicarboximide (NDI) and adjacent thiophene units is unfavorable to charge transport. Our group previously developed a new building block, the naphthalene bis(4,8-diamino-1,5-dicarboxyl)amide (NBA), by removing two carbonyl groups on the NDI unit, resulting a highly planar main chain with a small torsion angle of $\sim 10^\circ$. The resulting polymers showed excellent ambipolar transport capabilities. However, the removal of carboxyl groups raises high lowest unoccupied molecular orbital (LUMO) energy level, which is unfavorable to electron injection and transport.

To address this challenge, we are working on two complementary approaches. In the first (Figure 3), to further promote electron transport, we are attempting to lower the LUMO energy level through fluorine substitution. Interestingly, DFT computations indicate that difluorine substitution on NBA enables a lowering the LUMO energy level up to 0.25 eV with negligible effects on the backbone planarity. In recent developments, we demonstrated a promising synthetic strategy to achieve these new NDI building blocks and successfully characterize them. We are currently functionalizing these unit to enable cross-coupling reactions affording the corresponding polymers.

In the second strategy (Figure 4), we designed and synthesized the new building block NIA by removing one carbonyl group from NDI core. The resulting NIA-T2 show better planarity (see crystal structure in Figure. 4b) than NDI-T2 and lower LUMO energy level than NBA-T2 (-3.0 vs. -2.6 eV). To understand the structure-property relationship, we initially synthesized two new polymers similar with famous N2200 using NIA as electron accepting unit and di-thiophene as electron donating unit. Preliminary results indicate the TFTs based on PNIA-1, PNIA-2 show electrical properties with μ_e of 0.01, $0.1 \text{ cm}^2 \text{ V}^{-1} \text{ s}^{-1}$ in air. This study offering a chance to investigate the effects the number of carbonyl group on naphthalene to their electronic properties. Ongoing efforts are focused on synthesizing more NIA-based polymers by optimizing the electronic properties.

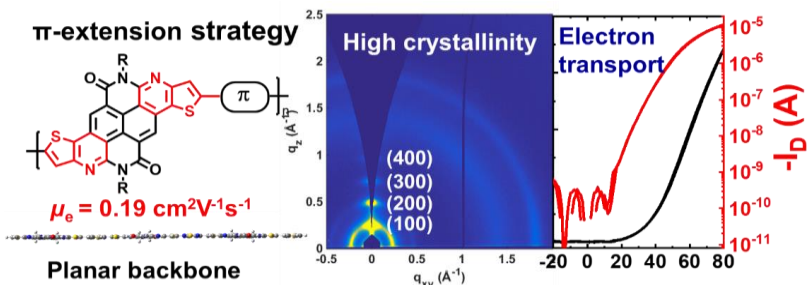


Figure 2. The molecular structure of TPNA-based polymers. (supported by DFT computation). Here excellent backbone planarity, high crystallinity and good electron transport ability were achieved for these polymers.

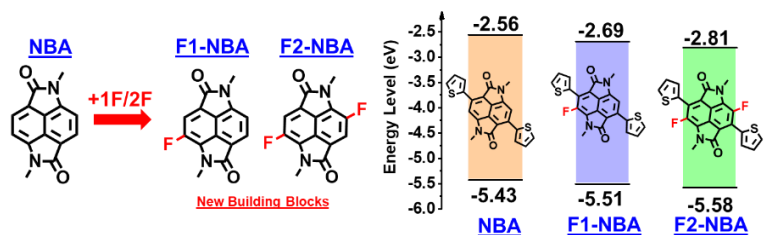


Figure 3. Chemical structure of new building blocks and measured energy levels of F-NBA-T2.

Finally, guidance of polymer design using molecular units as testbeds has been fundamental for new developments. In a recent study the first example of an *n*-type BTBT-based semiconductor,

D(Ph_FCO)-BTBT,

has been realized via a two-step transition metal-free process without using

chromatographic purification (**Figure 5**). Physicochemical and optoelectronic characterizations of the new semiconductor were performed in detail and the crystal structure accessed. The new molecule exhibits a large optical band gap (~2.9 eV) and highly stabilized ($\Delta E_{\text{LUMO}} = 1.54$ eV)/ π -delocalized LUMO mainly comprising the BTBT π -core and *in-plane* carbonyl units. The effect of *out-of-plane* twisted (64°) pentafluorophenyl groups on LUMO stabilization is found to be minimal. Polycrystalline **D(Ph_FCO)-BTBT** thin-films prepared by physical vapor deposition exhibit large grains (~2-5 μm sizes) and “layer-by-layer” stacked *edge-on* oriented molecules with an *in-plane* herringbone packing (intermolecular distances ~3.25-3.46 Å) to favor two-dimensional (2D) source-to-drain (S→D) charge transport. The corresponding TC/BG-OFET devices demonstrated high electron mobilities of up to 0.51 $\text{cm}^2/\text{V}\cdot\text{s}$ and $I_{\text{on}}/I_{\text{off}}$ ratios of 10^7 - 10^8 . These results demonstrate that the large band-gap BTBT π -core is a promising candidate for high mobility *n*-type organic semiconductors and, combination of very large intrinsic charge transport capabilities and optical transparency, may open a new perspective for next-generation unconventional optoelectronics. We are currently implementing this motif into polymers.

See: Usta, H.; Kim, D.; Ozdemir, R.; Zorlu, Y.; Kim, S.; Ruiz Delgado, M. C.; Harbuzaru, A.; Kim, S.; Demirel, G.; Hong, J.; Ha, Y.-G.; Cho, K.; Facchetti, A.; Kim, M.-G. High Electron Mobility in [1]Benzothieno[3,2-b][1]benzothiophene-Based Field-Effect Transistors: Toward *n*-Type BTBTs. *Chem. Mater.* **2019**, *31*(14), 5254-5263.

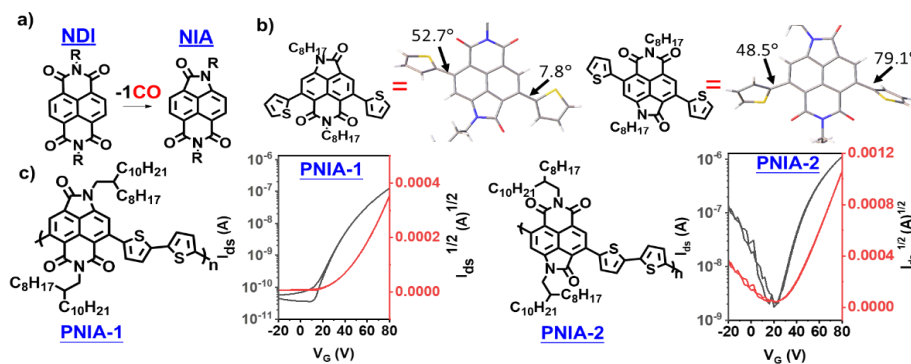


Figure 4. (a) Chemical structures of the new **NIA** building blocks. (b) Crystal structures of **NIA-T2** isomeric units showing different torsion. (c) Chemical structure of two representative NIA-based polymers and their corresponding I-V characteristics in a FET device demonstrating *n*-type character.

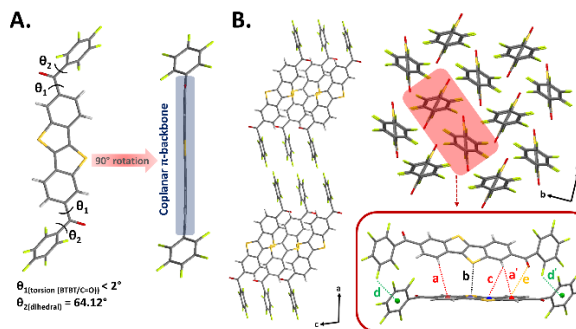


Figure 5. A. Capped-stick drawings of the crystal structure of **D(Ph_FCO)-BTBT** showing the corresponding dihedral and torsion angles and π -backbone coplanarity. B. Perspective views of the molecular arrangements along the *a,c*-axes and *b,c*-axes showing the alternately stacked layers and the two-dimensional herringbone-like packing, respectively. Inset shows the pairs of **D(Ph_FCO)-BTBT** molecules in a herringbone motif with $\text{CH}\cdots\pi$ (benzene/thiophene) ($a = 3.45$ Å; $a' = 3.25$ Å; $c = 3.46$ Å), $\text{S}\cdots\pi$ (thiophene) ($b = 3.38$ Å), and $\text{F}\cdots\pi$ (pentafluorobenzene) ($d = 3.30$ Å; $d' = 3.16$ Å) contacts.

N-type small molecules have traditionally exhibited lower transistor performance (e.g., field effect mobility) than the corresponding p-types. Thus, we also made advances in developing completely new n-type units, which could be incorporated into polymers. In a recent study a novel quinoidal thienoisindigo (TII)-containing small molecule family with dicyanomethylene end-capping units and various alkyl chains were synthesized as n-type organic small molecules for solution-processable OTFTs (**Figure 6**). The molecular structure of the 2-hexyldecyl substituted derivative, **TIIQ-b16**, was determined via single-crystal X-ray diffraction and showed that the **TIIQ** core is planar and exhibits molecular layers stacked in a “face-to-face” arrangement with short core intermolecular distances of 3.28 Å. The very planar core structure, shortest intermolecular N⋯H distance (2.52 Å), existence of an intramolecular non-bonded contact between sulfur and oxygen atom (S⋯O) of 2.80 Å and a very low-lying LUMO energy level of -4.16 eV suggest that **TIIQ** molecules should be electron transporting semi-conductors. We studied detail of the physical, thermal and electrochemical properties as well as OFETs performance and thin film morphologies of these new **TIIQs** (**Table 1**). Thus, air-processed **TIIQ-b16** OFETs exhibit an electron mobility up to 2.54 cm² V⁻¹ s⁻¹ with a current ON/OFF ratio of 10⁵~10⁶, which is the first demonstration of TII-based small molecules exhibiting unipolar electron transport and enhanced ambient stability. These results indicate that construction of quinoidal molecule from TII moiety is a successful approach to enhance n-type charge transport characteristics.

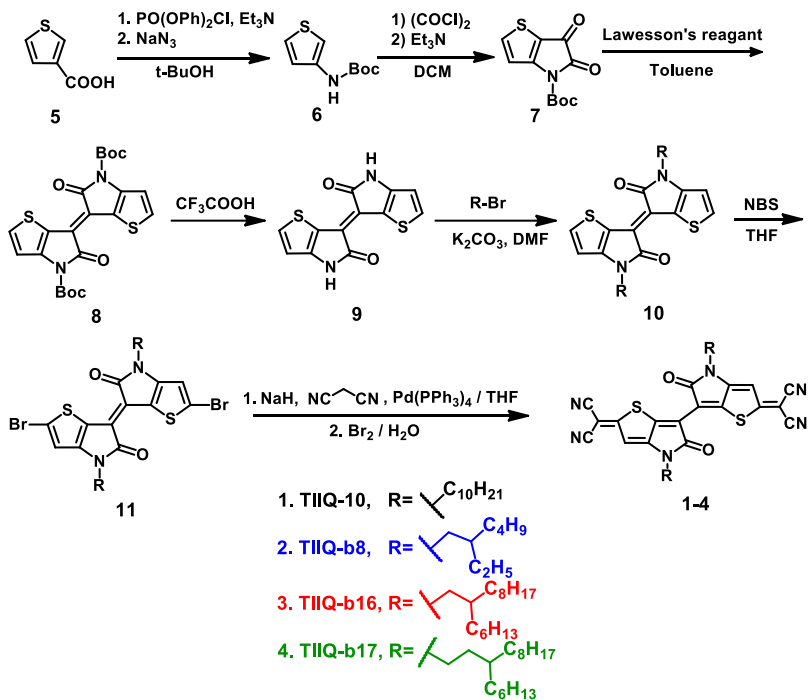


Figure 6. (Synthetic route to quinoidal molecules **TIIQ** (1-4).

as OFETs performance and thin film morphologies of these new **TIIQs** (**Table 1**). Thus, air-processed **TIIQ-b16** OFETs exhibit an electron mobility up to 2.54 cm² V⁻¹ s⁻¹ with a current ON/OFF ratio of 10⁵~10⁶, which is the first demonstration of TII-based small molecules exhibiting unipolar electron transport and enhanced ambient stability. These results indicate that construction of quinoidal molecule from TII moiety is a successful approach to enhance n-type charge transport characteristics.

Table 1. Summary of OFET parameters based on solution-sheared **TIIQs** thin films.

Compound	Thin film (//) ^{a)}				Thin film (⊥) ^{a)}			
	$\mu_{max}^{b)}$ [cm ² V ⁻¹ s ⁻¹]	$\mu_{avg}^{c)}$ [cm ² V ⁻¹ s ⁻¹]	I_{ON}/I_{OFF} [-]	$V_{th}^{b)}$ [V]	$\mu_{max}^{b)}$ [cm ² V ⁻¹ s ⁻¹]	$\mu_{avg}^{c)}$ [cm ² V ⁻¹ s ⁻¹]	I_{ON}/I_{OFF} [-]	$V_{th}^{b)}$ [V]
TIIQ-10	0.013	0.006±0.003	10 ³ ~10 ⁴	-6.61±3.89	0.009	0.005±0.002	10 ³ ~10 ⁴	-0.14±6.34
TIIQ-b8	0.792	0.462±0.165	10 ⁴ ~10 ⁵	-1.26±2.99	0.462	0.228±0.107	10 ⁴ ~10 ⁵	-4.39±3.96
TIIQ-b16	2.54	1.14±0.454	10 ⁵ ~10 ⁶	16.2±7.23	0.27	0.15±0.066	10 ⁵ ~10 ⁶	18.2±3.90
TIIQ-b17	0.195	0.113±0.035	10 ³ ~10 ⁴	-27.0±6.64	0.18	0.118±0.029	10 ³ ~10 ⁴	-33.6±3.26

^{a)}Charge transport direction is symbolized by // (parallel) and ⊥ (perpendicular) with respect to the solution-shearing direction; ^{b)}Maximum mobility; ^{c)}Average mobility.

See: Velusamy, A.; Yu, C.-H.; Afraj, S. N.; Lin, C.-C.; Lo, W.-Y.; Yeh, C.-J.; Wu, Y.-W.; Hsieh, H.-C.; Chen, J.; Lee, G.-H.; Tung, S.-H.; Liu, C.-L.; Chen, M.-C.; Facchetti, A., Thienoisindigo (TII)-Based Quinoidal Small Molecules for High-Performance n-Type Organic Field Effect Transistors. *Adv. Sci. (Weinheim, Ger.)* **2021**, 8 (1), 2002930.

P-type Polymers and Small Molecule-Polymer Blends. The identification of new building blocks for hole transport is of great importance to achieve structures bendable/stretchable implementable in several type of opto-electronic devices. In a recent demonstration, we reported a facile, high-yield synthetic access to the difluoro BTA building block, 4,7-bis(5-bromo-4-(2-hexyl-decyl)-thiophen-2-yl)-5,6-difluoro-2-(pentadecan-7-yl)-benzo[d]thiazole (BTAT-2f, **Figure 7**) for the realization of Donor (D)-Acceptor 1(A1)-

D-Acceptor 2(A2) polymers [D = bithiophene, A1 = BTA-2f, A2 = benzothiadiazole (BT) derivative] for use as a p-type semiconductor in transistors as well for organic solar cells (OSCs). Fine tuning of polymer optical and electronic properties is achieved by incrementally varying the A2 fluorination level. FET devices afford comparable hole mobilities of $\sim 0.1 \text{ cm}^2/\text{Vs}$. Bulk-hetero-junction (BHJ) PBTATBT-4f:Y6 sunlight-to-electricity cells deliver a noteworthy power conversion efficiency (PCE) of 16.08 % without processing additives. In contrast, PBTATBT-2f:Y6 exhibits an irregular morphology and low PCE, ascribable to the first demonstration

of co-crystal formation, which is unprecedented in such materials. This result is important since blend morphology degree of crystallinity can greatly influence mechanical properties.

See: Feng, L.-W.; Chen, J.; Mukherjee, S.; Sangwan, V. K.; Huang, W.; Chen, Y.; Zheng, D.; Strzalka, J. W.; Wang, G.; Hersam, M. C.; DeLongchamp, D.; Facchetti, A.; Marks, T. J.; Readily Accessible Benzo[d]thiazole Polymers for Nonfullerene Solar Cells with >16% Efficiency and Potential Pitfalls, *ACS Energy Letters*, **2020**, *6*, 1780 – 1787. DOI: 10.1021/acenergylett.0c0069.

In another p-type design strategy, we expanded our previously investigated hole transporting polymers based on the benzo[1,2-b:4,5-b']dithiophene moiety, to achieve polymers far more easy to synthesize and integrated them again into FETs. In fact, the best p-type polymers reported to date require laborious multiple synthetic steps due to their complex donor-acceptor architectures. Furthermore, record device performance relies on using halogenated solvents, e.g. chlorobenzene and chloroform as processing solvents, which are harmful to human health and the environment, and unacceptable for module manufacture. In addition, most of the high-efficiency devices are reported on small circuit and photoactive areas ($< 1 \text{ cm}^2$), raising the question of whether large performances are conserved when the polymers are implemented in large area devices. Therefore, simplification of the polymer donor chemical structure, reduction of the small-to-large area performance, and compatibility of the device fabrication procedure with industrial standards remain to be addressed. Recently we developed a series of readily accessible and scalable benzo[1,2-b:4,5-b']dithiophene (BDT)-2,5-dithienyl-thieno[3,4-c]pyrrole-4,6-dione (TPD-T2) based p-type polymers are utilized them in FET and sunlight-to-electricity cells (**Figure 8**). All polymers readily dissolve in chlorine-free solvents such as xylene, and the corresponding films can be processed in

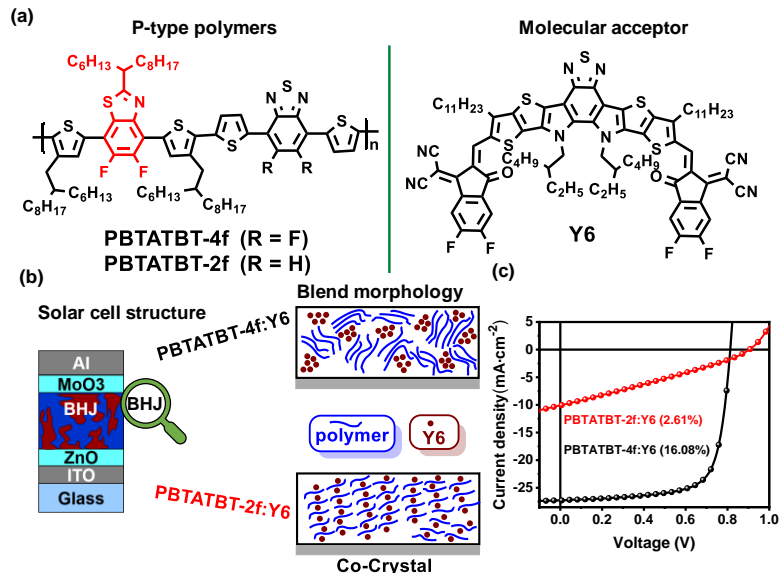


Figure 7. (a) Chemical structure of the p-type polymers and acceptor used in this study. (b) Inverted device architecture and schematic of PBTATBT-2f:Y6 blend film morphology. (c) J-V curves of photovoltaic devices.

ambient from this solvent to fabricate FETs and cells with hole mobilities $> 0.3 \text{ cm}^2/\text{Vs}$ and power conversion efficiencies (PCEs) $> 12\text{-}14\%$. Furthermore, the film processing and device metrics are remarkably insensitive to the processing methodology (spin-coating vs. blade coating), processing solvent, and the polymer molecular mass/dispersity index, results rationalized by UV-vis, PL, fsTA, AFM, TEM, GIWAX, and SCLC measurements. These properties enable the first light-to-electricity modules, processed in ambient from a benign solvent, with a certified PCE of 10.1% for an area of 20.4 cm^2 , and $> 7\%$ after light soaking. The same module also delivers a power of $\sim 40 \mu\text{W}/\text{cm}^2$ (PCE $\sim 22\%$) under indoor lighting. This work represents an important step in materials development for fabricating/manufacturing large-scale devices with extremely high figures of merit, inferring that they can reach commercialization. Currently we are carrying out mechanical stress tests on circuits to understand their tensile properties.

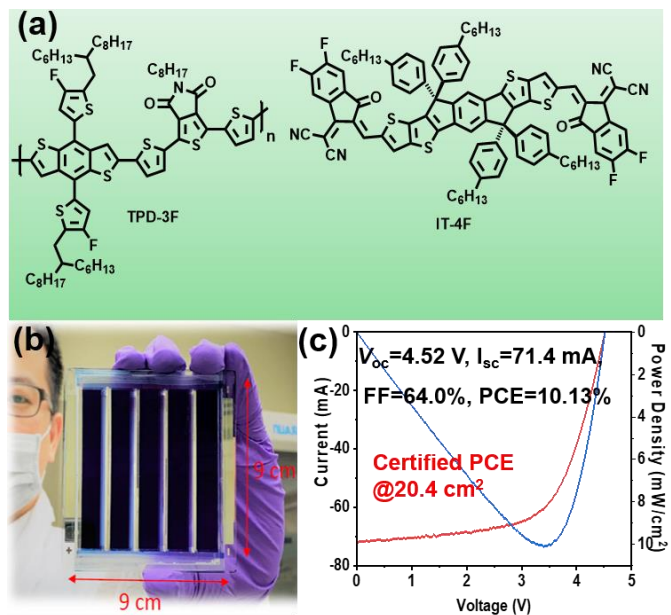


Figure 8. (a) Chemical structures of the TPD polymers and acceptor employed in this study. (b) Photograph of TPD-3F based light-to-electricity module. (c) and D. I-V characteristics of the module (module area = 20.4 cm^2) measured under AM 1.5G solar irradiation at an intensity of $100 \text{ mW}/\text{cm}^2$.

See: Liao, C.; Chen, Y.; Lee, C.; Wang, G.; Teng, N.; Lee, C.; Li, W.; Chen, Y.K.; Li, C.; Ho, H.; Tan, P.; Huang, Y.; Young, R.M.; Wasielewski, M.R.; Marks, T.J.; Chang, Y.; Facchetti, A.; Large Area Non-Fullerene Organic Photovoltaic Module with a Record Power Conversion Efficiency $> 10\%$, *Joule*, **2020**, *4*, 189-206. DOI:10.1016/j.joule.2019.11.006.

A strategy to improve film morphology, degree of texture, solution processability, and thus charge transport of small molecules semiconductors, including n-(hetero)acenes, is by blending them with an insulating amorphous polymer. To achieve high OFET performance the phase separation and crystallization of the small molecule/insulating polymer blend must be appropriately manipulated. State-of-art blend-based OFETs are generally processed by spin-coating, which waste most of the semiconductor formulation, and using highly toxic halogenated solvents. Additionally, it has been shown that charge carrier mobilities are strongly dependent upon the blend composition with the greatest performance achieved around 1:1 weight ratio. Thus, it would be desirable to investigate blends more forgiving to the polymer content variation and using more semiconductor saving processing methodologies. In a recent paper we explore the blends of the new molecular semiconductor **DDTT-DSDTT (1)** (Figure 9), based on the **DSDTT** core. This molecule exhibits intramolecular locks using S...S interactions as accessed in previous studies on similar molecules

preliminary result, we are working on these soft polymers for the ambipolar devices in intrinsically stretchable electronics.

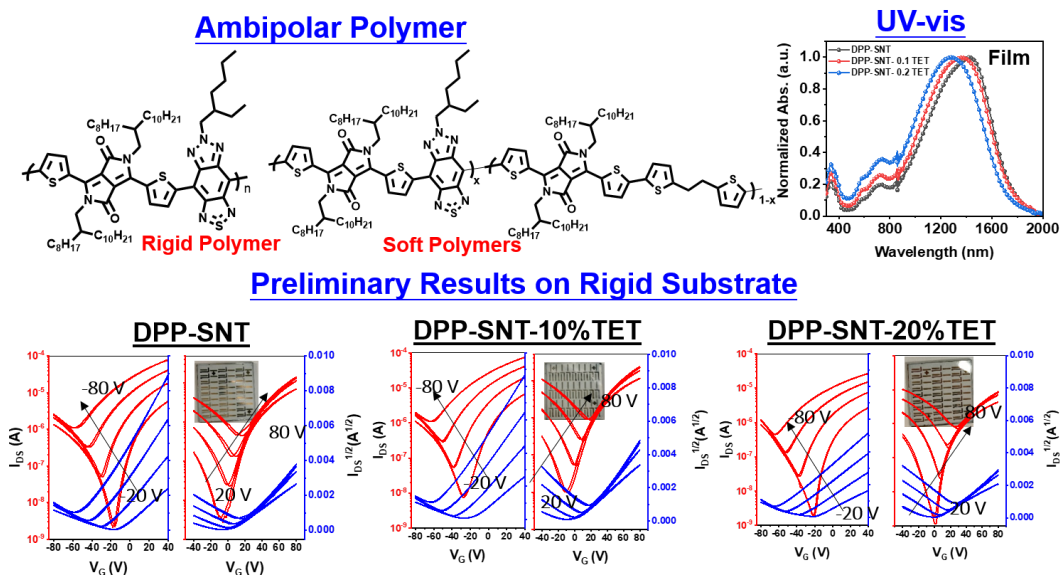


Figure 10. Top. Chemical structure of the achieved polymers. Bottom. UV-vis spectra and I-V characteristics.

See: Chen Y.; Zhuang X., Huang W., Facchetti A., Marks T. J. Printable Organic-Inorganic Nanoscopic Multilayer Gate Dielectrics for Thin-Film Transistors Enabled by a Polymeric Organic Interlayer. *Ready for submission*.

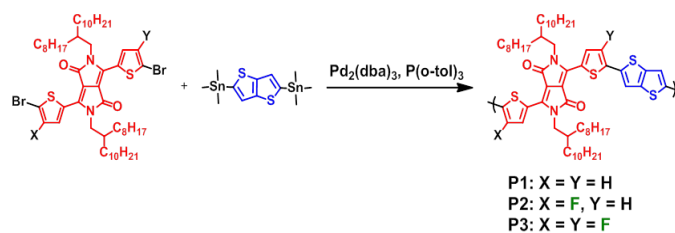


Figure 11. Synthesis of the new DPP Polymers.

In another strategy to achieve ambipolarity, we carried out the synthesis and characterization of a series of fluorinated 3,6-di(thiophen-2-yl)pyrrolo-[3,4-c]pyrrole-1,4(2H,5H)-dione (TDPP) monomers and polymers (**Figure 11**). An array of physicochemical techniques including optical spectroscopy, electro-chemistry, and diverse solid-state characterization techniques are used to characterize the TDPP monomer and polymer properties. It is found that successive TDPP fluorination incrementally lowers the FMO energies and redshifts the optical spectra. A dramatic change in TDPP unit crystal packing from herringbone columns to a slip-stack brickwork pattern also occurs on moving from nonfluorinated (**T₂DPP**) and monofluorinated (**^FT₂DPP**) building blocks to the difluorinated (**^FT₂DPP**) unit. The solid state packing is strongly affected by intermolecular F···H interactions in the molecular crystal (**Figure 12**). The fluorinated units are then used to synthesize the corresponding, alternating donor-acceptor copolymers. Solution-cast films of the fluorinated copolymers exhibit strong aggregation and crystallinity as assessed by AFM

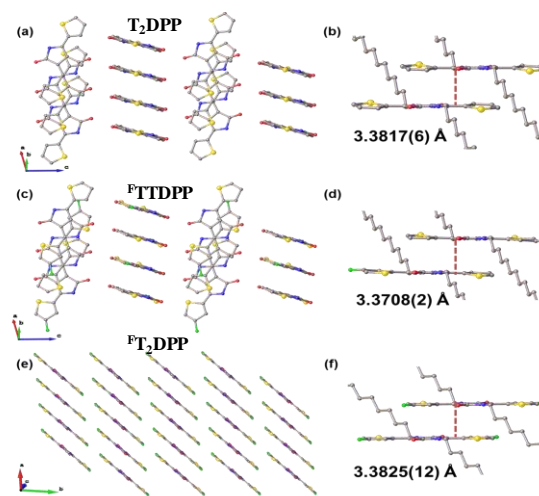


Figure 12. Crystal structure of the DPP units with different fluorine contents.

images and 2D grazing incidence wide angle X-ray scattering. Importantly, the polymer with the highest fluorine content (poly(3,6-bis(4-fluorothiophen-2-yl)-2,5-bis(2-octyldodecyl)pyrrolo-[3,4-c]pyrrole-1,4(2H,5H)-dione-*alt*-thieno[3,2-*b*]thiophene) has the closest π - π stacking distances and the longest crystalline domain correlation length of 3.80 Å and 48.4 Å, respectively. Top-gate bottom-contact field-effect transistors were fabricated and evaluated for this polymer series. These devices operate in both *p*- and *n*-channel regimes with ambient-stable hole mobilities exceeding $1 \text{ cm}^2 \text{ V}^{-1} \text{ s}^{-1}$ for spin-coating films. Recent experiments in polymer chain alignment results in $\sim 5x$ larger mobilities. The properties of these fluorinated semiconductors demonstrate that fluorinated TDPPs are attractive for future opto-electronic materials development.

See: Leonardi, M.J.; Melkonyan, F.S.; Fabiano, S.; Barger, C.J.; Wang, G.; Manley, E.F.; Mouat, A.R.; Chen, L.X.; Facchetti, A.; Marks, T.J.; Sequential Thienyldiketopyrrolopyrrole Fluorination: Modulation of Physicochemical Properties and Optoelectronic Device Performance, In preparation.

Sustainable Synthesis and Processing using new Reactions and Solvents

Conjugated polymer synthesis by direct arylation polymerization. The production of high-performance semiconducting small molecules and polymers hinges critically on developing atom-efficient chemistries which produce the desired materials with low defect density and with negligible toxic byproducts such as those used in conventional Stille reactions (Figure 13). To this end, catalytic direct C–H arylation polymerization (DARP) holds great promise, however those

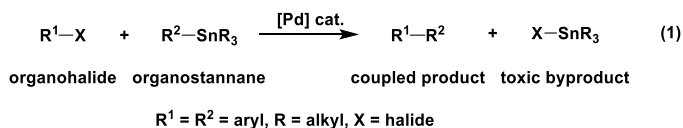


Figure 13. Building blocks used for conventional Stille synthesis producing toxic byproducts.

factors controlling the C–H arylation regioselectivity for substrates containing multiple reactive aryl C–H bonds are not well understood, nor are their photovoltaic consequences. Here, we mechanistically scrutinize defect formation pathways occurring during the DARP synthesis of an archetypal, commonly-used, π -conjugated donor-acceptor benzodithiophene-*alt*-diketopyrrolopyrrole copolymer, **PBDTT-DPP**. DARP-derived copolymer properties including molecular mass, dispersity, optical cross-section, and device (FET, OSC) performance are shown to be dramatically sensitive to the polymerization reaction conditions (Figure 14), however standard spectroscopic characterization methods are alone inadequate to identify or quantify the trace device-performance-altering defects. Instead, small molecule model studies analyzed by HPLC-

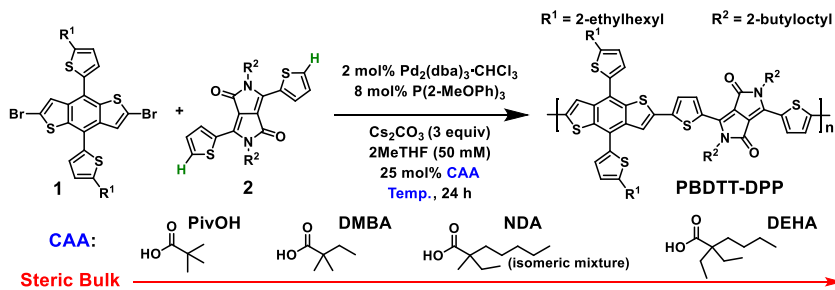


Figure 14. Building blocks and conditions used for DARP synthesis.

HRMS are employed to untangle the effects of DARP reaction parameters on trace chemical defect (primarily hydrodehalogenation and β -C–H arylation) formation outcomes (Table 2). Consequently, the influence of trace defects on PSC performance is clarified and enables the identification of branching arising from non-selective C–H functionalization at incorrect sites on both comonomers as the principal photovoltaically deleterious defect. Using this information to fine-tune the polymerization reaction temperature and carboxylic acid catalyst additive significantly reduces branching densities to below 1%, with an exceptional C–H regioselectivity of $>110:1$ under optimal DARP conditions. The optimal

copolymers achieve superior device performance versus defect-rich DARP-derived copolymers and rival those from organotin waste-producing Stille polycondensations.

Table 2. Synthetic details and properties of Stille vs. DARP reactions.

Batch	CAA	Temp. (°C)	Copolymer	Yield (%)	M_n (kg/mol) ^b	\mathcal{D}^b	λ_{\max} (nm) ^c	A_{0-0}/A_{0-1}^d
1 ^e	-	-	Stille	91	34.1	3.97	773, 704^f	2.02
2		75	75-P-24	76 ^g	21.4	5.40	771, 703 ^f	1.70
3	PivOH	80	80-P-24	25 ^g	16.4	4.82	770, 702 ^f	1.61
4		85	85-P-24	35 ^g	14.5	5.49	770, 702 ^f	1.58
5		90	90-P-24	42 ^g	15.6	11.20	769, 702 ^f	1.53
6		75	75-DMB-24	96	20.9	4.05	772, 703 ^f	1.73
7	DMBA	80	80-DMB-24	28 ^g	17.3	4.74	771, 703 ^f	1.68
8		85	85-DMB-24	34 ^g	18.2	5.13	771, 703 ^f	1.68
9		90	90-DMB-24	20 ^g	14.9	5.86	770, 702 ^f	1.60
10		75	75-ND-24	95	18.9	3.26	771, 703 ^f	1.75
11	NDA	80	80-ND-24	94	20.9	3.63	771, 703 ^f	1.75
12		85	85-ND-24	92	24.7	4.15	771, 703 ^f	1.75
13		90	90-ND-24	94	19.4	4.73	771, 703 ^f	1.71
14		75	75-DEH-24	94	21.4	3.30	772, 703 ^f	1.77
15	DEHA	80	80-DEH-24	96	23.1	3.62	772, 703 ^f	1.77
16		85	85-DEH-24	89^g	23.2	4.04	771, 703^f	1.76
17		90	90-DEH-24	83	21.4	4.59	771, 703 ^f	1.74

^a Reaction Conditions: **1** (0.1 mmol), **2** (0.1 mmol), Pd₂(dba)₃·CHCl₃ (2 mol%), P(2-MeOPh)₃ (8 mol%), Cs₂CO₃ (3 equiv), CAA (25 mol%) in 2MeTHF (2.00 mL) at indicated temperature for 24 h. Yields for copolymer isolated from chlorobenzene Soxhlet extraction. ^b Determined by GPC at 150 °C in TCB. ^c Solution absorption spectra in 1,2-dichlorobenzene (DCB, 0.01 mg/mL). The first quantity corresponds to absorption peak maximum or vibronic A₀₋₀ band. ^d Absorbance maximum intensity relative to absorbance shoulder. ^e Reference copolymer synthesized via Stille polycondensation. ^f Absorbance shoulder or vibronic A₀₋₁ band. ^g Some copolymer not extractable with chlorobenzene.

See: Aldrich, T. J.; Zhu, W.; Mukherjee, S.; Richter, L. J.; Gann, E.; DeLongchamp, D. M.; Facchetti, A.; Melkonyan, F. S.; Marks, T. J. Stable Postfullerene Solar Cells via Direct C-H Arylation Polymerization. Morphology-Performance Relationships. *Chem. Mater.* **2019**, *31*, 4313-4321.

Biomass-derived processing solvents for organic semiconductors. Despite remarkable achievements in terms of organic semiconductor (OSC)-based device electrical performance, reliability and stability, far less efforts addressed the needs to overcome the use of hazardous halogenated/aromatic solvents for their realization. The solvent choice for the OSC-based device fabrication process is crucial to achieve optimal performance since it affects the self-assembly/aggregation of the OSC in solution and during film formation, thus ultimately, the TFT channel film morphology and charge transport characteristics. We recently reported on the very wide selection of green solvents to process organic semiconductors (**Figure 15**) to provide evidence that a more sustainable solvent and materials combination is possible for the fabrication of OFETs. To realize green solvent-processable TFTs with high figures-of-merit, the organic semiconductor should form a favourable morphology upon the cast of the given solvent. Additionally, the solvents should afford enough solubility for the semiconductor material (> ~1 mg/mL), possess suitable boiling point, and viscosity. Therefore, besides the greenness requirement, we have optimized solvent selection based on the above criteria, using a bottom-gate/top-contact device geometry. Our results demonstrate that devices from several green solvents exhibit comparable/higher field-effect mobilities than

those from conventional chlorobenzene, 1,2-dichlorobenzene, chloroform, *o*-xylene, and toluene processing. Thus, a hole mobility $> 1.0 \text{ cm}^2\text{V}^{-1}\text{s}^{-1}$ was obtained for several solvents such as diethyl succinate, isobutyl acetate, dimethyl carbonate, and *t*-amyl methyl ether. Particularly, the TIPS PEN devices processed from isobutyl acetate exhibit a remarkable μ up to $2.6 \text{ cm}^2\text{V}^{-1}\text{s}^{-1}$ with a $I_{\text{on}}:I_{\text{off}} > 10^4$. Furthermore, as a proof-of-concept, we employed a green solvent-processed combination of a semiconductors and a cellulose-cinnamate dielectric (Figure 15b) for the demonstration of a more sustainable OTFT technology.

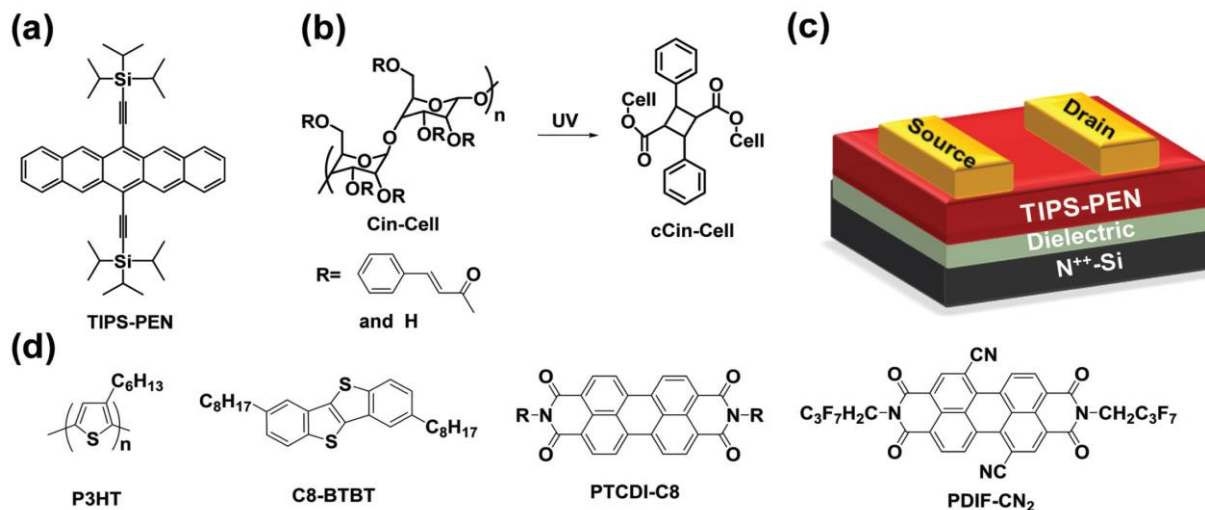


Figure 15. Chemical structure of (a) TIPS-PEN semiconductor; (b) cellulose cinnamate (Cin-Cell) dielectric precursor and the corresponding UV-promoted curing process to afford the cross-linked gate dielectric (cCin-Cell); (c) bottom-gate/top-contact (BG/TC) TFT geometry used for screening green solvents. (d) Chemical structure of additional p- and n-type semiconductors used in this study.

See: Ho, D.; Lee, J.; Park, S.; Park, Y.; Cho, K.; Campana, F.; Lanari, D.; Facchetti, A.; Seo, S.; Kim, C.; Marrocchi, A.; Vaccaro, L. Green solvents for organic thin-film transistor processing. *J. Mater. Chem. C* **2020**. DOI: 10.1039/D0TC00512F

Polymer-Inorganic Composite Semiconductors

Metal oxide (MO) semiconductors, particularly the amorphous ones, have proven great advantages compared to silicon because of the greater charge transport properties in the amorphous state and the possibility to fabricate thin films from solution under ambient conditions. However, MO films are poorly bendable and cannot be stretched. Thus, based on previous results from our group, we have undertaken approaches using polymers to enhance the mechanical robustness of these semiconductors as well as to find additives to process their films from solution at lower temperatures.

New co-fuels for reducing combustion polymer-oxide synthesis temperatures. Our group has pioneered a general strategy for fabricating solution-processed metal-oxide TFTs at dramatically lower temperatures (as low as 200 °C for all TFT electrical components) using self-energy generating combustion synthesis (CS). Combustion synthesis, driven by the exothermic reaction of a liquid fuel+oxidizer+ metal precursor, has become an important methodology for growing amorphous and polycrystalline metal oxide (MO) films as well as MO-polymer semiconducting composites (vide infra). This approach was used to fabricate flexible, transparent TFTs on several plastic substrates. qualitative structure-property relationship between

the resulting MO film composition/microstructure and charge transport characteristics. In optimized MO CS precursors the fuel combines a primary coordinating ligand [e.g., acetylacetonate (AcAc)] with an additional cofuel (e.g., a carbohydrate). Several studies suggest a qualitative structure-property relationship between the resulting MO film composition/microstructure and macroscopic charge transport characteristics. Nevertheless, the details of the precursor coordination chemistry remain poorly defined. Here we select chemically and compositionally different cofuels (urea, glycine, sorbitol, L-ascorbic acid) and explore the mechanistic details of fuel-assisted combustion synthesis focusing on the technologically important MO semiconductor, indium gallium zinc oxide (IGZO) as the platform (**Figure 16**). Thermogravimetric analysis and differential scanning calorimetry, ^1H NMR, mass spectrometry, and x-ray diffraction are used to probe how the cofuel affects AcAcH-metal ion coordination and influences the

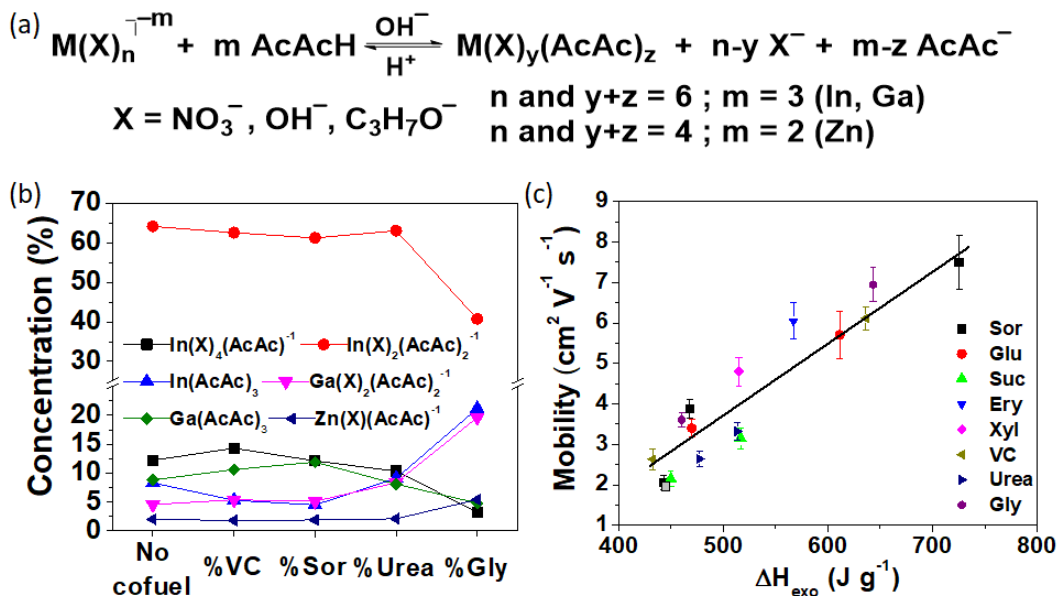


Figure 16. (a) Chemistry of combustion synthesis. (b) Concentration dependence of the indicated species after 10wt% cofuel addition. η_{H} is the concentration of the indicated precursor species. (c) Plot of FET mobility vs. combustion enthalpy (ΔH_{exo}) for FACS IGZO TFT systems

MO precursor thermal response. The charge transport characteristics of these cofuel-derived IGZO films stimulated additional cofuel studies with glucose, sucrose, erythritol, and xylitol; the results support the general role of the cofuel in intensifying CS heat generation, hence IGZO film microstructure densification and carrier mobility. These results provide new insight into precursor coordination chemistry and its relationship to thin-film combustion processes, yielding information for selecting more efficient, environmentally benign (co)fuels for solution-processed MO electronics.

See: Wang, B.H.; Leonardi, M.J.; Huang, W.; Chen, Y.; Zeng, L.; Eckstein, B.J.; Marks, T.J.; Facchetti, A.; Marked Cofuel Tuning of Combustion Synthesis Pathways for Metal Oxide Semiconductor Films, *Advanced Electronic Materials*. **2019**, 5, 1900540. DOI: 10.1002/aelm.201900540.

Scalable and printable combustion synthesis of metal oxides. We recently addressed an important barrier to roll-to-roll manufacturing of solution-processed MO materials. In fact, MO semiconductor thin films prepared from solution typically require multiple hours of thermal annealing to achieve optimal lattice densification, efficient charge transport, and stable device operation, which is difficult to be implemented into a production FAB line. Thus, we developed a new, highly efficient cofuel-assisted combustion blade

coating (CBC) process for MO film growth which involves introducing both a fluorinated fuel and a pre-annealing step to remove deleterious organic contaminants and promote complete combustion (**Figure 17**). Ultrafast reaction and metal–oxygen–metal (M–O–M) lattice condensation then occur within 10–60 sec at 200–350 °C for representative MO semiconductor (indium oxide, In_2O_3 ; indium zinc oxide, IZO; indium gallium zinc oxide, IGZO) and dielectric (aluminum oxide, Al_2O_3) films.

Thus, ultrafast reaction and metal–oxygen–metal (M–O–M) lattice condensation then occur within 10–60 sec at 200–350 °C for a representative MO semiconductors (indium oxide; indium zinc oxide; indium gallium zinc oxide) and dielectric (alumina) films. Scalable CBC fabrication of IGZO- Al_2O_3 TFTs (60 sec anneal) with FET mobilities as high as $\sim 25 \text{ cm}^2 \text{ V}^{-1} \text{ s}^{-1}$ and negligible threshold voltage deterioration in a

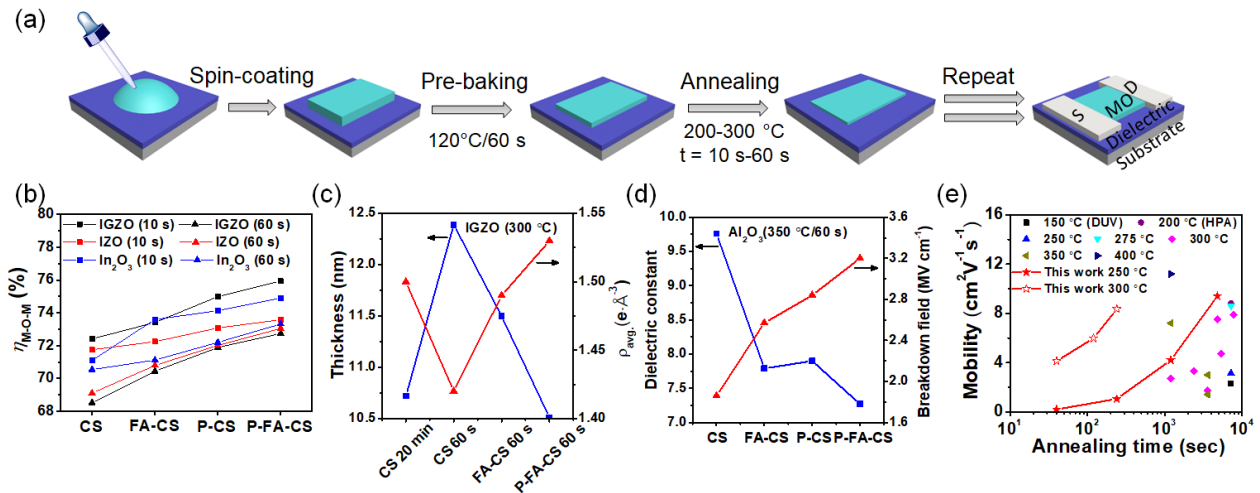


Figure 17. (a) Film-fabrication processes with the schematic evolution of MO-precursor coordination chemistry and film thickness. (b) Ratio of O(1s) X-ray photoelectron spectroscopic M–O–M peak area to total peak area for In_2O_3 , IZO, and IGZO films subjected to the indicated processing. (c) Film thickness and average electron density of IGZO films processed by the indicated methods. (d) Calculated dielectric constant (10^3 Hz) and BF for 350 °C-annealed CS, FA-CS, P-CS, and P-FA-CS Al_2O_3 dielectric films. (e) Comparison with literature data for solution-processed IGZO TFT mobilities on 300-nm SiO_2/Si vs. annealing time

demanding 4000 sec bias stress test are realized (**Figure 18**). Combined with polymer dielectrics, the CBC derived IGZO TFTs on polyimide substrates exhibit high flexibility when bent to a 3 mm radius, with performance bending stability over 1000 cycles.

See: Wang, B.; Guo, P.; Zeng, L.; Sil, A.; Huang, W.; Leonardi, M.J.; Zhang, X.; Wang, G.; Yu, X.; Bedzyk, M.J.; Schaller, R.D.; Marks, T.J.; Facchetti, A.; Ultrafast, scalable fabrication of solution-processed metal oxides for thin-film electronics, *PNAS*, **2019**, *116*, 9230–9238. DOI: 10.1073/pnas.1901492116.

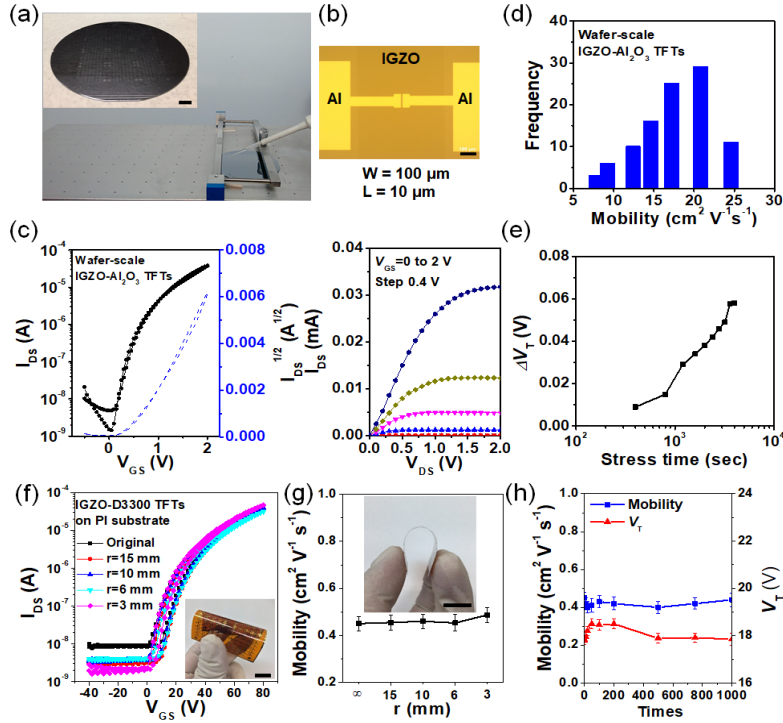


Figure 18. Scalable combustion blade coating (CBC) fabrication of high-performance IGZO TFTs on both high- k Al_2O_3 dielectrics and low- k polymer dielectrics. (a) Photo of blade-coating (BC) process; inset shows blade-coated devices on a 4" Si wafer. Scale bar = 1 cm. (b) Optical image of a patterned low-voltage IGZO TFTs. Scale bar = 100 μm . (c) Transfer and output characteristics of low-voltage CBC IGZO TFT on high- k Al_2O_3 dielectrics. The annealing time for both IGZO and Al_2O_3 layers is 60 sec. (d) Distribution of saturation mobilities and (e) ΔV_t vs. time of CBC/FA-CS-derived IGZO TFTs on $\text{Al}_2\text{O}_3/\text{Si}$ substrates ($V_{\text{GS}} = +1.0$ V). (f) Transfer curves and (g) mobility variation of top-gate flexible CBC/IGZO TFTs on a polyimide (PI) substrate as a function of bending radius. Inset: photo of device under bending; scale bar = 1 cm. (h) Mobility and threshold voltage stability for bending test cycles with radius = 6 mm.

Polymer-metal oxide semiconductor blends. The mechanical properties of pristine metal oxide TFTs on plastic substrates, regardless if the MO semiconductor film is amorphous or polycrystalline, rapidly degrade when they are subjected to bending. However, as we discussed in our proposed efforts, we discovered that by adding an insulating polymer such as PVP or PVA into the combustion MO precursor solution, it is possible to achieve amorphous oxide phases and In_2O_3 TFTs with much greater mechanical stability. The drawback of this approach was that upon polymer addition the mobility of these TFTs monotonically decreases

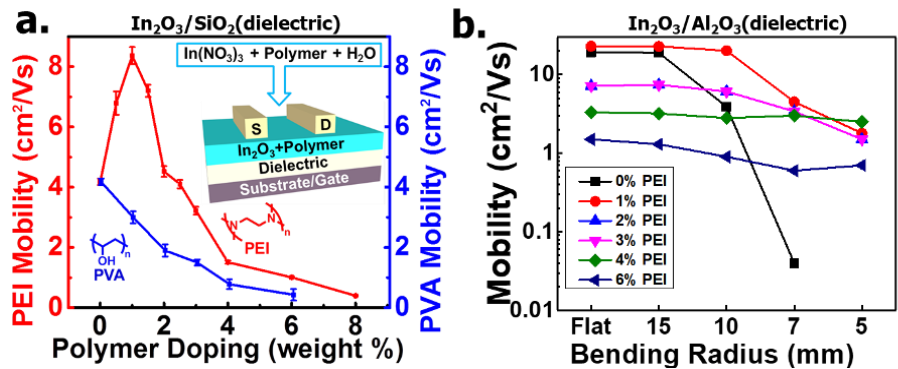


Figure 19. a. Mobility-polymer loading in polymer- In_2O_3 blends. b. Mobility-bending radius dependence for the indicated blends.

when the PVP concentration increases. More recently, we discovered that using optimal loadings of the electron-rich polymer, polyethylenimine (PEI), affords superior TFT performance, including higher electron mobility than that of the pristine In_2O_3 matrix (**Figure 19a**). Furthermore, recently, we discovered that when the PEI content increases, the mechanical properties increase and the mobility dependence of the corresponding TFTs with mechanical stress falls (**Figure 19b**).

However, PEI has a large content of amine nitrogen atoms (%N), $\sim 34\%$ and it is not a very stable polymer. Thus, an interesting question is what the role of %N versus that of the polymer structure on the doping efficiency of In_2O_3 :polymer blends and how it affects charge transport and the mechanical properties of the corresponding thin films and TFTs. To address this question we investigated the synthesis of In_2O_3 :polymer blends based on four amino-polymers, as well as their mixtures, with progressively reduced N% (**Figure 20**)--specifically, PEI (12.6%), poly(allylamine) (PAA, 9.1%), polyethylenimine ethoxylated (PEIE, 6.9%), and poly(4-vinylphenol)-block-poly[2-(4-vinylphenoxy)ethan-1-amine] (PVP-NH₂, 2.6%) as well as investigate blend morphology, electronic structure, and charge transport in TFT architectures vis-à-vis PVP (0%).

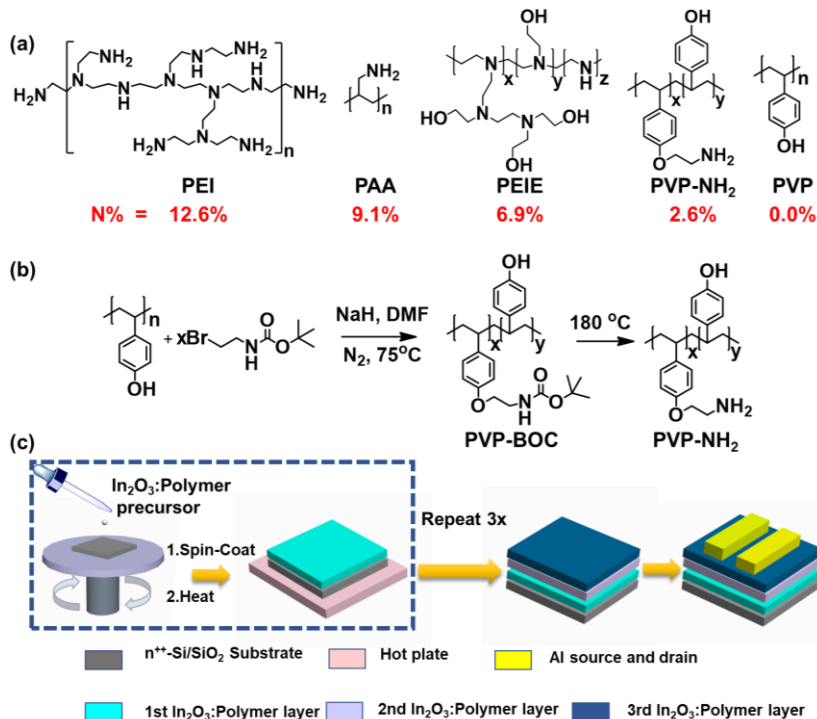


Figure 20. (a) Structures of PEI, PAA, PEIE, PVP-NH₂, and PVP. (b) Synthesis process of PVP-BOC and thermolysis of PVP-BOC to PVP-NH₂ at 180 °C. (c) Schematic of the In_2O_3 :polymer blend film fabrication process and TFT structure used in this study.

The results demonstrated that the doping capacity of the polymers and the TFT blend mobility correlates not only with N% and the polymer weight loading in the precursor formulation, systematically varied here from 0 to 2 wt.%, but also with the polymer thermal stability and the carbon content of the resulting In_2O_3 films (**Figures 21 and 22**). Thus, all amino-polymers, including PVP-NH₂ with a N% of only 2.6%, efficiently donate electrons to the MO (In_2O_3) matrix. Moreover, a general trend is that the TFT performance enhancement, as quantified by the peak mobility (μ_{peak}) in **Figure 21** and the mobility variation vs. pristine In_2O_3 (**Figure 23a**) indicates that all polymers with a substantial N% content ($> 7\%$) are effective in enhancing μ_{peak} by $\sim +80\%$ while far lower metrics are obtained for PVP-NH₂ (N% = 2.6%), where the mobility increase is far lower ($\sim +40\%$). However, for the polymer having no amine nitrogen, PVP (N% = 0%), the mobility decreases by $\sim -40\%$. Noe, PAA (N% = 9.1%) is an exception with a μ_{peak} and mobility increase far lower (only $\sim 10\%$) than the other N-rich polymers, likely reflecting the considerable carbon content in the films (accessed by XPS), which is greater than that of PVP-NH₂. Indeed, when using a PEIE/PEI mixture (1:0.63 in weight) affording the same N% as that of PAA (9.1%) in the In_2O_3 precursor solution, the corresponding TFTs exhibit a remarkable μ_{peak} enhancement of $\sim 87\%$ (see black arrow in

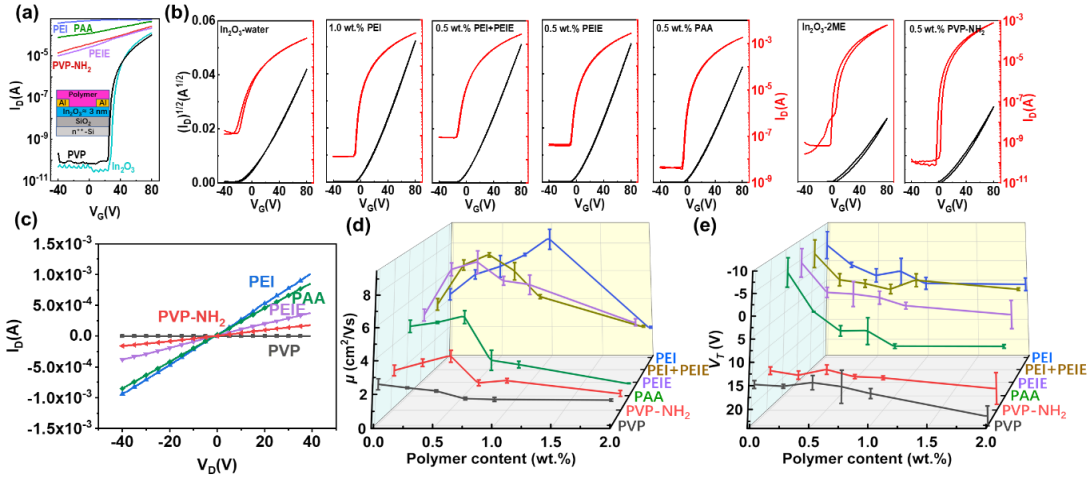


Figure 21. (a) Transfer curves from the indicated device structures (insert) having different wt% polymer coatings ($V_D = +80$ V). (b) Representative transfer curves of transistors based on the indicated In_2O_3 : polymer blend films. (c) I_D - V_D curves for the indicated polymers at $V_G=0$. (d) Mobilities and (e) threshold voltages for TFTs based on In_2O_3 : polymer blend films from precursors having different polymer contents. In panel e it is clear that all N-containing polymers exhibit a peak in mobility (μ_{peak}) for a N content ~ 0.5 -1%

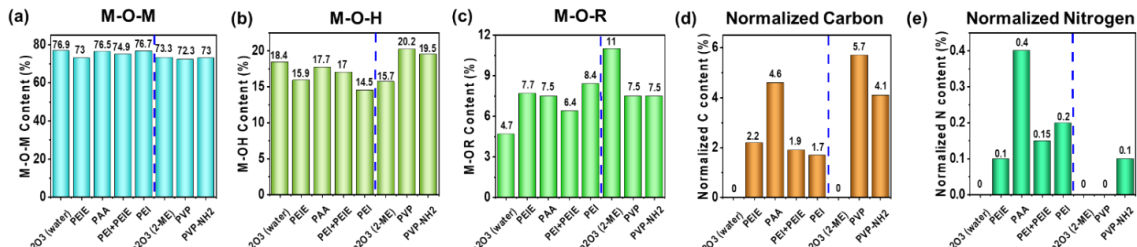


Figure 22. M-O-M (a), M-O-H (b), M-O-R (c) content for films of 0.5 wt.% different polymer doped In_2O_3 and normalized C content (d) and N content (e) of 2 wt.% polymer doped In_2O_3 .

Figure 23a). Similarly, UPS measurements of the PEIE/PEI derived In_2O_3 indicate that the film WF is considerably below that of the film from the PAA-containing precursor formulation (black arrow in **Figure 23b**), despite identical N% in the polymer additive. Thus, from these results, we postulate that not only the polymer N% plays an important role in controlling charge transport, but also the residual carbon in the blend after processing strongly influences the electron transport efficiency. Thus, polymers having electron-donating sites but not thermolyzing efficiently, such as PAA, yield higher carbon residue densities, which would likely compromise the electrical performance of the conducting metal oxide matrix.

To address whether using N-containing polymers raise filled states to higher energies and whether there is a correlation of N% in the polymer structure, UPS measurements were performed to assess the In_2O_3 :polymer blend WFs (**Figure 23b**). Note that these films were processed in the same way as employed for TFT fabrication but using ITO coated glass as the substrate. As shown in **Figure 23b**, the WFs of the polymer doped In_2O_3 films depend on the polymer type and content, shifting from 4.16 eV for pristine In_2O_3 (both water or 2-ME processed) to 3.98 eV and 3.94 eV for 0.5 wt.% and 1.0% PEI, respectively, while PVP does not affect the WF which remains at ~ 4.16 -4.17 eV for 0.5 wt.% and 1.0 wt.% PVP content. Overall, shallower WFs are obtained for polymers having higher N% and greater matrix polymer content, again, with the exception of PAA. PAA incorporation is far less effective in reducing the WF than PEIE and PEI, and increasing the PAA content shifts the WF to a far less than the other two amine-rich polymers [4.04 eV (0.5 wt.% PAA) and 4.02 eV (1.0 wt.% PAA)]. PAA WF values are statistically identical to those of N-poor PVP-NH₂, where increasing this polymer content is detrimental to the WF [4.02 eV (0.5 wt.%

PVP-NH₂) and 4.06 eV (1.0 wt.% PVP-NH₂)]. Thus, the UPS data clearly demonstrate that significant C contamination lowers the N-doping capacity of the N-containing polymers, in accord with the experimental variation of the TFT performance trends in **Figures 21 and 23a**. Thus, excessive more traps than the electron-donating N atoms can fill during precursor conversion to the metal oxide film.

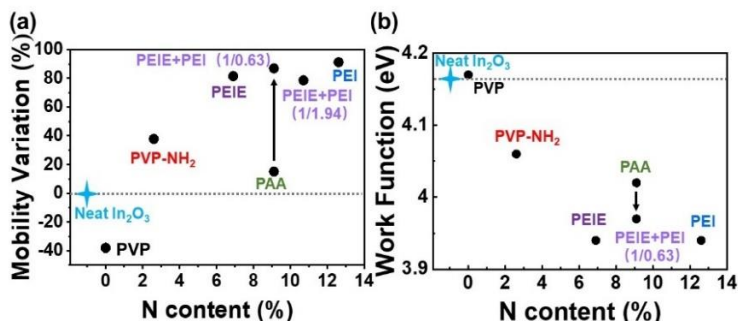


Figure 23. TFT mobility maximum variation vs. N% (a) and work function (WF) vs. N% (b) for the indicated blends. Note, for (a) the peak mobility maximizes at a polymer content of 0.5-1.0 wt.% while for (b) all WF values measured for a 1.0 wt.% polymer content. Similar trends are obtained for 0.5 wt.%.

We also surveyed how polymer doping and structure affect the mechanical properties of In₂O₃:polymer blend TFTs. Mechanically flexible devices were fabricated on polyimide (PI) substrates using Cr/Au gate contacts covered with F:AIO_x films as the gate dielectric and, after In₂O₃:polymer blend film deposition, and Al source/drain electrodes (structure in **Figure 24a**). This dielectric film exhibits a stable capacitance over a wide frequency range, and TFTs using this dielectric exhibit reliable carrier mobilities and negligible *I*-*V* hysteresis. All the present flexible TFTs on PI substrates show good transistor response at low operating voltages, $V_G = -1$ to 2 V for $V_D = -2$ V, and provide higher mobilities than on Si/SiO_x substrates. Importantly, the In₂O₃:polymer blend TFTs exhibit greater mechanical stress tolerance than those based on pure In₂O₃ (**Figures 24b-d**). These findings provide a powerful tool to modulate oxide film electronic and mechanical properties, leading to high performance TFTs with excellent mechanical flexibility, as well as shed light on how the particular polymer tunes MO semiconductor charge transport.

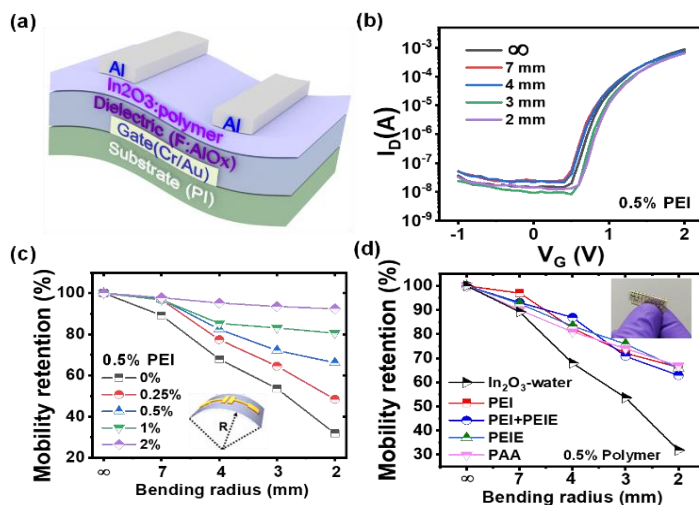


Figure 24. (a) Flexible TFT structures used in this study, (b) representative I-V curves of 1 wt.% PEI doped In₂O₃ flexible TFTs at different bending radii, (c) mobility-bending radius dependence of In₂O₃: polymer bend TFTs with different PEI contents, and (d) having no or 0.5 wt.% of polymer content.

See: Wang, Z.; Zhuang, X.; Wang, B.; Huang, W.; Marks, T.J.; Facchetti, A.; Doping Indium Oxide Films with Amino-Polymers of Varying Nitrogen Content Markedly Affects Charge Transport and Mechanical Flexibility, **2021**, in press. DOI: 10.1002/adfm.202100451.

More impressively, we recently discovered that the field-effect electron mobility of aqueous solution-processed indium gallium oxide (IGO) thin-film transistors is significantly enhanced by polyvinylalcohol (PVA) addition to the precursor solution, > 70-fold increase to 7.9 cm²/Vs, which is among the highest mobilities reported for solution-processed IGO films (**Figure 25**). Note PVA cannot donate electrons as PEI; thus these exceptional data opened new fundamental questions and can provide an alternative routes to mechanically flexible MO-polymer blends. To understand the way PVA operates, IGO:PVA film microstructure, electronic structure, and charge transport were investigated by a battery of experimental and theoretical techniques, including In K-edge and Ga K-edge EXAFS, R-SoXS, UPS, FT-IR spectroscopy, ToF-SIMS, composition/processing dependent TFT response, high-resolution solid state ¹H, ⁷¹Ga, and ¹¹⁵In NMR spectroscopy, and DFT analysis with *ab-initio* MD liquid-quench simulations. The ⁷¹Ga{¹H REDOR NMR and other data indicate that PVA achieves optimal H doping with a Ga··H distance of ~3.4 Å and conversion from 6 to 4-coordinate Ga, which together suppress deep trap defect localization.

This reduces metal-oxide polyhedral distortion, thereby increasing the electron mobility. This result not only offers a new route to high-performance, ultra-stable metal oxide semiconductor electronics with simple binary compositions, but also provides powerful tools to probe H locations in polymer-doped amorphous metal oxides via a combination of experimental and theoretical approaches.

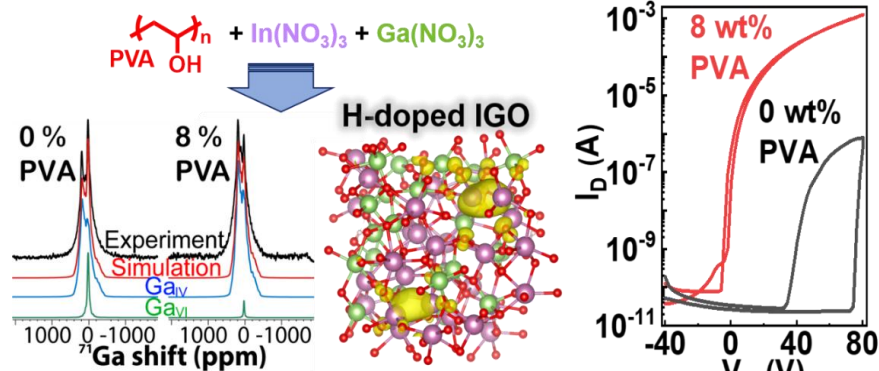


Figure 25. PVA incorporation in IGO precursor leads to conversion of Ga from 6 to 4-coordination, and optimized H sites, which suppress deep trap defect localization and tremendously enhanced IGO semiconducting property.

See: Huang, W.; Cen, P.H.; McMillen, K.; Tedesco, J.; Zeng, L.; Mukherjee, S.; Wang, B.; Chen, Y.; Gang, W.; Wang, Y.; Gao, Y.; Bedzyk, M.J.; DeLongchamp, D.; Hu, Y.Y.; Medvedeva, J.E.; Marks, T.J.; Facchetti, A.; Experimental and Theoretical Evidence for Hydrogen Doping in Polymer Solution Processed Indium Gallium Oxide, *PNAS* **2020**, *117*, 18231-18239. DOI:10.1073/pnas.2007897117.

Dielectric Materials

In this Task we are developing new gate dielectrics designed to improve our understanding of TFT transport-dielectric structure relationships, enhance the gate capacitances for low voltage/power operation, maintain/increase carrier mobility, and be compatible with printing processes as well as with flexible substrates.

Polymeric self-assembled nanodielectrics (P-SAND)s. In previous studies, we clearly demonstrated that small-molecule based self-assembled nanodielectrics (SANDs) offer an excellent combination of high capacitance and low operating voltage. In addition, SANDs are compatible with a wide range of semiconductors including oxides, organics, hybrid organic-inorganic, and nanomaterials. However, SAND

processing is not currently compatible with printing and the mechanical robustness has not been explored. To address these points, we designed polymeric SANDs (P-SANDs) consisting of stilbazolium units linked to a polymeric backbone. We recently showed that P-SAND synthesis is possible and the polymer can be anchored to a surface functionalized with a coupling agent (**Figure 26**). The organic SAND component, named P-PAE, consists of a polarizable π -electron phosphonic acid-based unit implemented on a polymeric backbone. Thus, the new polymer SANDs (PSANDs) films can be deposited both by spin-coating and blade-coating in air by alternating assembling P-PAE, a capping reagent layer, and an ultrathin ZrO_x layer. The new PSANDs thickness varies from 6 to 15 nm depending on the number of organic-ZrO_x bilayers, exhibit tuned film thickness, well-defined nanostructures, large electrical capacitance (up to 558 nF/cm²), and good insulating properties (leakage current densities as low as 10⁶ A/cm²). Organic thin-film transistors (OTFTs) fabricated with various p/n- type organic molecular/polymeric semiconducting materials,

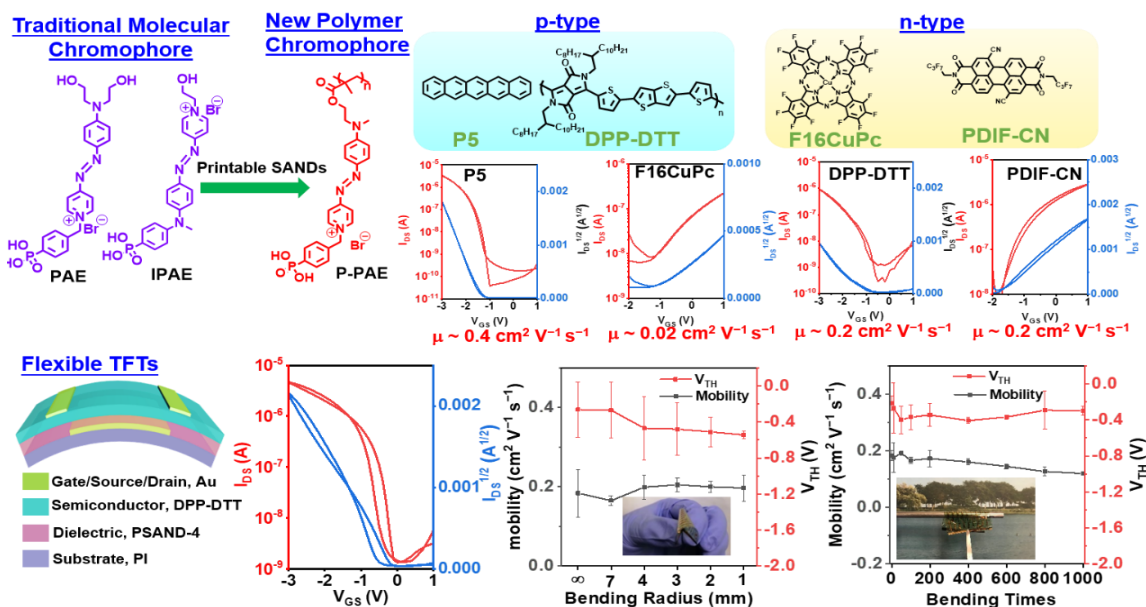


Figure 26. Structures of PSAND dielectric chromophores/semiconductors, I-V characteristics, and electrical properties on flexible TFTs.

function well at low voltages (< 3.0 V). Furthermore, flexible TFTs by using PSAND exhibit excellent mechanical flexibility and good bias stress stability, demonstrating a promising route to low-voltage operation flexible electronics. Finally, printable PSANDs were also demonstrated and affords TFTs with electrical properties comparable with those achieved with the spin-coated PSAND-based devices.

See: Chen, Y.; Zhuang, X.; Huang, W.; Facchetti, A.; Marks, T.J.; Printable Organic-Inorganic Nanoscopic Multilayer Gate Dielectrics for Thin-Film Transistors Enabled by a Polymeric Organic Interlayer. *Advan. Funct. Mater.* **2020**, *30*, 2005069. DOI:10.1002/adfm.202005069

Top-Gated Transistor Architectures Enabled by SANDs. Two promising solution phase approaches we recently developed for the low-temperature growth of high-performance dielectric and semiconductor films are, respectively, the self-assembly of organic-inorganic hybrid nanodielectrics (SANDs) and the combustion synthesis of metal oxides. SANDs feature nanolayers of inorganic oxide dielectrics such as

SiO_x, ZrO_x, and HfO_x, interleaved with highly polarizable conjugated organic molecules, e.g., phosphonic acid derivatives of stilbazolium salts, which undergo self-assembly onto the inorganic nanolayers. This

urable materials platform provides high gate capacitances in TFT devices, lower gate leakage currents than the neat solution-processed inorganic films, chemical and thermal stability, suppression of trapped charge, radiation hardness, and dielectric thicknesses ideal for device scaling. Combustion synthesis of metal oxide films has been shown to lower the processing temperature requirements for the growth of diverse semiconducting oxides, including In₂O₃, In-Zn-O, and In-Ga-Zn-O (IGZO). This is achieved by including an oxidizer (e.g., NO₃⁻) and a fuel (acetylaceton) in the oxide precursor solution, which promotes a highly exothermic film growth reaction, thereby achieving efficient oxide network condensation and C impurity removal. The broad compatibility of SANDs with diverse semiconductors has been demonstrated with pentacene, printed IGZO, graphene, and carbon nanotubes. These pairings yield impressive TFT mobilities and other device metrics. Top-gated TFT devices offer many attractions over bottom-gate architectures, especially for metal oxide semiconductors. Oxides are well known to react with atmospheric oxygen and water, and top-gated structures enable the dielectric to passivate the oxide surface by functioning as an encapsulation layer, thus making device response more uniform.

Top-gate IGZO TFTs have been reported with several classes of insulators including polymers and metal oxides. Polymer dielectrics offer mechanical flexibility and solution processing at low temperatures; however they typically exhibit low dielectric constants (k), excessive gas/H₂O permeability, and limited thermal stability. Inorganic dielectrics offer high- k s and environmental stability but generally require either capital-intensive vacuum deposition or high annealing temperatures, which can compromise the underlying semiconductor. While solution-processed SANDs combine many of the attractions of both inorganic and organic dielectrics and minimize many of their limitations, they have never been implemented in top-gated devices due to fabrication challenges. In recent work we demonstrated the first use of solution-processed SANDs in top-gate bottom-contact (TG-BC) oxide TFT structures (**Figure 27**). We first established that SANDs can be grown successfully on combustion-processed a-IGZO films while preserving well-defined nanostructures, as verified by optical spectroscopy (UV-Vis), AFM, X-ray reflectivity (XRR), and cross sectional-TEM measurements. In addition, Hf-SAND dielectric properties are assessed in metal-insulator-metal device structures via impedance spectroscopy. Finally, top-gate a-IGZO/Hf-SAND TFTs are fabricated and are shown to exhibit impressive device metrics such as a $\mu_{\text{SAT}} = 19.4 \pm 0.5 \text{ cm}^2 \text{ V}^{-1} \text{ s}^{-1}$, $V_{\text{th}} = 0.83 \pm 0.04 \text{ V}$, $\log(I_{\text{on}}:I_{\text{off}}) = 4.26 \pm 0.31$, and $\text{SS} = 293 \pm 22 \text{ mV/dec}$.

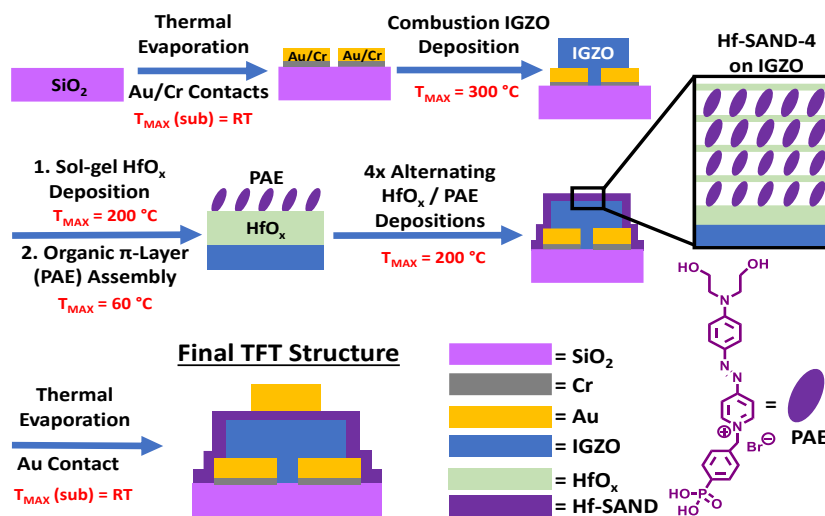


Figure 27. Fabrication scheme for top-gate a-IGZO/Hf-SAND-4 TFTs. The maximum processing temperature of each step is indicated. Note that components are not drawn to scale.

In recent work we demonstrated the first use of solution-processed SANDs in top-gate bottom-contact (TG-BC) oxide TFT structures (**Figure 27**). We first established that SANDs can be grown successfully on combustion-processed a-IGZO films while preserving well-defined nanostructures, as verified by optical spectroscopy (UV-Vis), AFM, X-ray reflectivity (XRR), and cross sectional-TEM measurements. In addition, Hf-SAND dielectric properties are assessed in metal-insulator-metal device structures via impedance spectroscopy. Finally, top-gate a-IGZO/Hf-SAND TFTs are fabricated and are shown to exhibit impressive device metrics such as a $\mu_{\text{SAT}} = 19.4 \pm 0.5 \text{ cm}^2 \text{ V}^{-1} \text{ s}^{-1}$, $V_{\text{th}} = 0.83 \pm 0.04 \text{ V}$, $\log(I_{\text{on}}:I_{\text{off}}) = 4.26 \pm 0.31$, and $\text{SS} = 293 \pm 22 \text{ mV/dec}$.

See: Stallings, K.; Smith, J.; Chen, Y.; Zeng, L.; Wang, B.; Di Carlo, G.; Bedzyk, M.J.; Facchetti, A.; Marks, T.J.; Self-Assembled Nanodielectrics for Solution-Processed Top-Gated Amorphous IGZO Thin Film Transistors, *ACS Appl. Mater. Interfaces* **2021**, *13*, 15399–15408. DOI: 10.1021/acscami.1c00249

UV-Fabricated SANDs at Room Temperature. SANDs can be fabricated by either vapor or solution processes. However, the most advanced SANDs, which include high- k metal oxide and stilbazolium-phosphonate layers, require a thermal annealing process (≥ 150 - 400 °C) for optimal operation. Such thermal

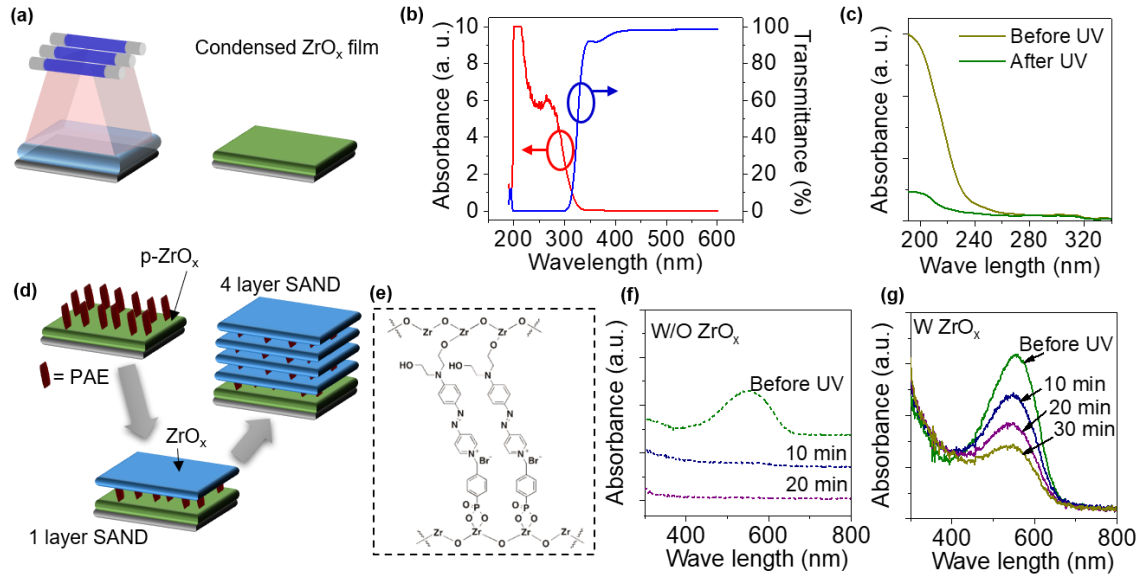


Figure 28. (a) Schematic representation of ZrO_x film fabrication by UV irradiation. (b) Absorbance and transmittance spectra of a ZrO_x precursor solution. (c) molecular structure of the PEI organic component of SAND. (d) Fabrication procedure of zirconia self-assembled nano-dielectric (Zr-SAND-n) multilayers. (e) Absorbance spectra of spin-coated ZrO_x precursor film before and after UV irradiation. (f) Absorbance spectra of a prime-ZrO_x-PAE film without the ZrO_x capping layer before and after irradiation. (g) Absorbance spectra of a Zr-SAND-1 before and after UV irradiation as well as after 300 °C thermal annealing.

annealing limits SAND compatibility with many plastic or bio-compatible substrates and restricts applications such as in bio-integrated electronics. Recently ultraviolet (UV) photochemical irradiation has been used to promote decomposition of metal oxide precursors to enable M-O-M lattice formation and film densification, thus avoiding thermal annealing. Since for SAND fabrication the step requiring high temperature annealing is that associated with the metal oxide layer densification, we investigated whether photochemical irradiation could be used to produce high-quality SANDs near room temperature and, equally importantly, the stability of the organic component under irradiation. Thus, we reported on the growth, structural, and dielectric properties as well as implementation in TFTs, of zirconium oxide based SANDs (Zr-SANDs) using UV irradiation processing (**Figure 28**). These newly produced dielectric films were characterized by x-ray reflectivity (XRR), atomic force microscope (AFM), and X-ray photoelectron spectroscopy (XPS), all of which demonstrate excellent film morphology and microstructure. The near room temperature fabricated Zr-SAND also exhibit excellent dielectric characteristics such as high capacitances (>700 nF/cm²), low leakage current density (J , $\sim 10^{-7}$ A/cm²), and very high performance uniformity (deviation $< 5\%$). Pentacene-based organic TFTs with these Zr-SANDs as gate dielectrics exhibit a mobility of 0.58 cm²V⁻¹s⁻¹ at 2 V demonstrating for the first time the realization of high-performance solution processed self-assembled multilayer dielectrics with minimal thermal annealing.

See: Huang, W.; Yu, X.; Zeng, L.; Wang, B.; Takai, A.; Di Carlo, G.; Bedzyk, M.; Marks, T.J.; Facchetti, A.; Ultraviolet Light Densified Oxide-Organic Self-Assembled Dielectrics. *Processing Thin Film*

Carbohydrate-derived photocrosslinkable dielectric materials. Photocurable dielectric films play an important role in modern optoelectronics and are crucial for the development of advanced TFTs and circuits. We recently explored a facile photoresist-free patterning method using natural carbohydrates for their use as OTFT gate dielectrics. The effect of the crosslinkable unit chemical structure on the crosslinking chemistry and dielectric strength of the corresponding films was explored by investigating cinnamate (Cin)-functionalized carbohydrates ranging from a monomer (glucose) to a dimer (sucrose) to a polymer

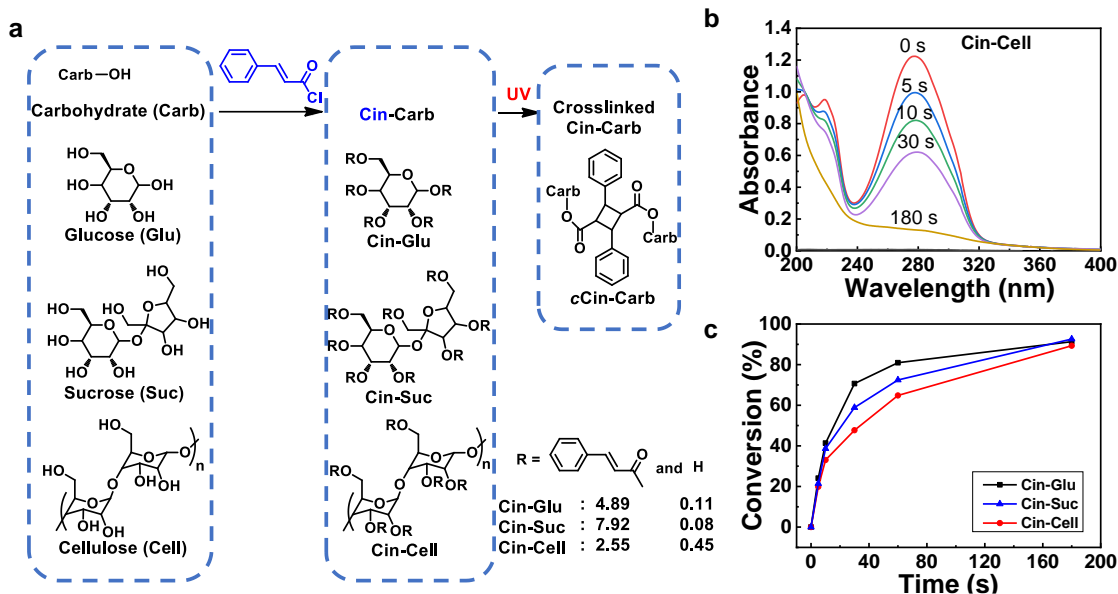


Figure 29. (a) Synthesis of cinnamate esters of the indicated carbohydrates and corresponding UV-promoted crosslinking process. (a) UV-vis spectra of Cin-Cell films on quartz substrates after different UV curing times. (b) Conversion degrees vs. curing time of Cin-Carbs.

(cellulose) (**Figure 29a**). Optical absorption measurements demonstrate that the UV light irradiation results in a [2+2] cycloaddition, converting the soluble precursors into a crosslinked carbohydrate network (**Figure 29b, c**). These films were characterized by UV-vis, FTIR, and XPS. Impedance spectroscopy shows that the crosslinked films are good dielectrics with $k = 3.5\text{--}3.7$ (at 1 kHz) and leakage currents of $2\text{--}7 \times 10^{-6}$ A/cm² at 1.5 MV/cm. Pentacene (p-type) and *N,N'*-1H, 1H-perfluorobutyl dicyanoperylene-carboxydiimide (PDIF-CN₂, n-type) TFTs were fabricated as testbeds for the new dielectric films. The best devices, based on crosslinked cellulose, exhibit mobilities similar to the control TFTs using rigid SiO₂ as the gate insulator. Finally, we demonstrated that Cin-cellulose can be efficiently patterned at low dosage using a biomass-derived solvent, resulting in stable and high-performance p- and n-type TFTs (**Figure 30**).

See: Wang, Z.; Zhuang, X.; Chen, Y.; Wang, B.; Huang, W.; Marks, T.J.; Facchetti, A.; Cinnamate-Functionalized Natural Carbohydrates as Photopatternable Gate Dielectrics for Organic Transistors, *Chem. Mater.*, **2019**, *31*, 7608-7617. DOI: 10.1021/acs.chemmater.9b02413.

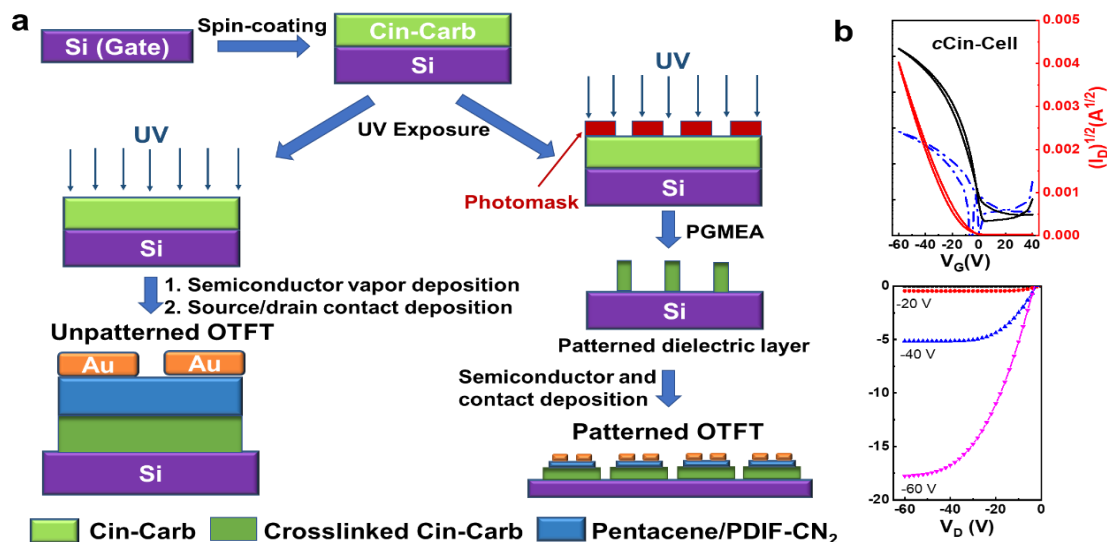


Figure 30. (a) Illustration of the OTFT device fabrication process (left: without patterned dielectric and semiconductor; right: with patterned dielectric and semiconductor). (b) Representative electrical characteristics of cellulose cinnamate gate dielectric based TFTs using pentacene as the semiconductor.

Modeling of new Type of Molecular Dielectrics. Quantum phenomena, such as constructive and destructive interference, significantly influence coherent electronic phenomena in organic semiconducting circuitry, including single-molecule junction devices, which are the principal subjects of this work. It is known that molecular wires comprised of (i) meta-substituted phenylene rings and (ii) cross-conjugated double bonds (orthogonal to the molecular long axis), can dramatically reduce electrical transmission. Here, added to these tools the use of a heretofore unexplored molecular shape to create quantum interference: a fully-conjugated molecular wire with a structure that is forced back on itself in a z-shape, thereby exhibiting remarkably low conductance ($G = 0.43 \times 10^{-9}$ S), even though the phenylene arrangements are *ortho*- rather than *meta*-disposed (**Figure 31**). We call these z-shaped molecules with ultra-low conduction: Z-Ortho-Regio-Resistive Organics (ZORROs). Here we analyzed the mechanism by which ZORRO molecules have significant insulating properties in the coherent electron transport regime due to destructively interfering transmission pathways in the phenylene rings (strong decoherence). We also found that ZORRO structures can be fine-tuned by derivatization. Curiously, both electron-withdrawing (fluorine) and electron-donating (methoxy) substituents enhance transmission. The former is due to destructive quantum interference suppression at the F site, thereby enhancing transmission, much like a Buttiker probe. In contrast, the methoxy unit is akin to a resonance additive and positively contributes to the transmission. Lastly, we examined the effects of replacing the phenylene rings with disubstituted thiophene rings, and how this significantly modulates the transmission based on a well-defined double-bond orientation. An

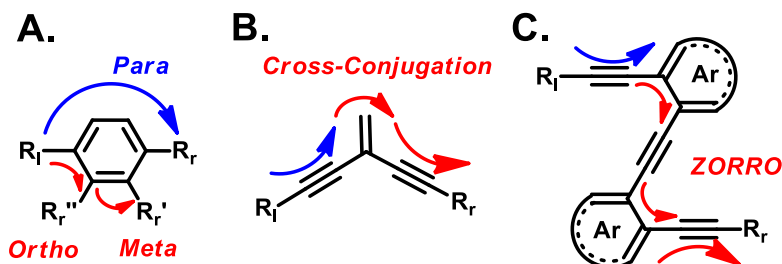


Figure 31. (A) Electrical transmission permitted (blue arrows) and inhibited (red arrows) with the *ortho* or *meta*-related substituents around a phenylene ring; (B), *cross-conjugation* of a molecular wires; (C), ZORRO insulating structure, R_l = terminal groups to left electrode, R_r = terminal groups to right electrode, Ar = aromatic rings.

z-shaped molecules with ultra-low conduction: Z-Ortho-Regio-Resistive Organics (ZORROs). Here we analyzed the mechanism by which ZORRO molecules have significant insulating properties in the coherent electron transport regime due to destructively interfering transmission pathways in the phenylene rings (strong decoherence). We also found that ZORRO structures can be fine-tuned by derivatization. Curiously, both electron-withdrawing (fluorine) and electron-donating (methoxy) substituents enhance transmission. The former is due to destructive quantum interference suppression at the F site, thereby enhancing transmission, much like a Buttiker probe. In contrast, the methoxy unit is akin to a resonance additive and positively contributes to the transmission. Lastly, we examined the effects of replacing the phenylene rings with disubstituted thiophene rings, and how this significantly modulates the transmission based on a well-defined double-bond orientation. An

ultra-low conductance of 0.13×10^{-9} S and a relatively high dielectric constant of ~ 5 is predicted with one thiophene ZORRO derivative, which closely resembles a double cross-conjugated unit, making it an excellent candidate for quantum interference field-effect transistors (QuFETs).

See: Jones, L.O.; Mosquera, M.A.; Fu, B.; Schatz, G.C.; Marks, T.J.; Ratner, M.A.; Quantum Interference and Substantial Properties Tuning in Conjugated Z-Ortho-Regio-Resistive Organic (ZORRO) Junctions, *NanoLetters*, **2019**, *19*, 8956-8963. DOI: 10.1021/acs.nanolett.9b03849.

Processing Semiconducting Polymers.

Mixed-flow microfluidic printing. The rational creation of two-component conjugated polymer systems with high levels of phase purity in each component is challenging but crucial for realizing printed soft matter electronics. Here we report a mixed-flow microfluidic printing (MFMP) approach for two-component polymer systems that significantly elevates phase purity in devices such as thin-film transistors and bulk-heterojunction solar cells and (Figure 32). MFMP integrates laminar and extensional flows using a specially microstructured shear blade, designed with fluid flow simulation tools to tune the flow patterns and induce shear, stretch, and push-out effects. This optimizes polymer conformation and semiconducting blend order as assessed by AFM, TEM, GIWAXS, R-SoXS, sunlight-to-electricity response, and field effect mobility. For printed all-polymer (J51:N2200) sunlight-to-electricity cells this approach enhances short-circuit currents and fill factors, with power conversion efficiency increasing from 5.20 % for conventional blade-coating to 7.80 % for MFMP. Moreover, the performance of mixed polymer ambipolar (P3HT:N2200) and semiconducting:insulating polymer unipolar (N2200:polystyrene) transistors is similarly enhanced, underscoring versatility for two-component π -polymer systems. Mixed flow designs offer new modalities for achieving high-performance organic opto-electronics via innovative printing methodologies.

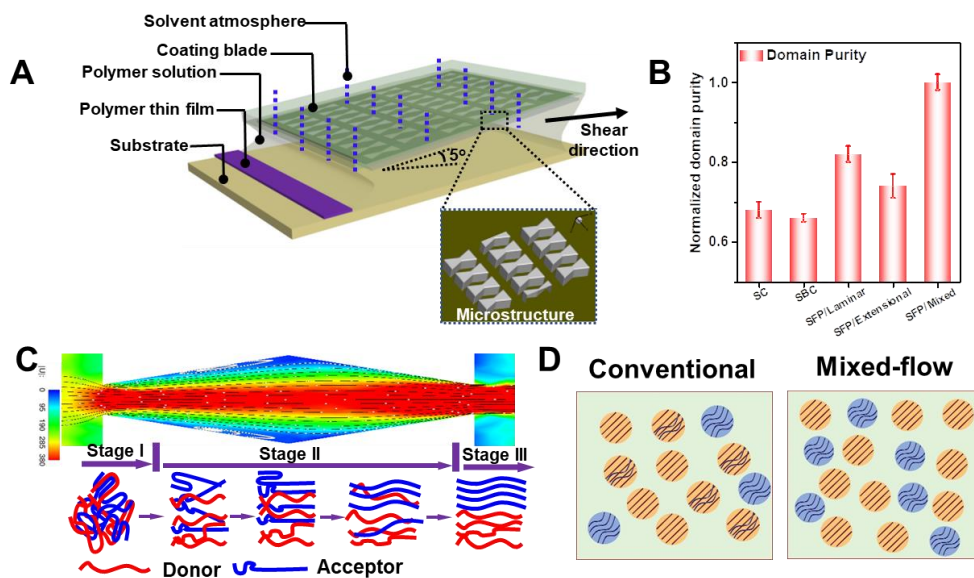


Figure 32. The mixed-flow design for two-component polymer semiconductor systems. (A) The Schematic of the fabrication process implemented on the solution shearing platform; (B) domain purity obtained from integration of R-SoXS peaks that follow material contrast; Error bars for variations were estimated from peak fits to profiles acquired at several energies in the range 283-284 eV where the material contrast is optimum. (C) The hypothesized polymer conformational change, alignment and pure domain formation in the shear field. (D) Schematic illustration of the possible in-plane morphology (The illustration is simplified, focusing on the domain purity/crystallinity information, and the domain connectivity is not shown).

See: Wang, G.; Feng, L.; Huang, W.; Mukherjee, S.; Chen, Y.; Shen, D.; Wang, B.; Strzalka, J.; Zheng, D.; Melkonyan, F. S.; Yan, J.; Stoddart, J. F.; Fabiano, S.; DeLongchamp, D.; Zhu, M.; Facchetti, A.; Marks, T. J.; **Mixed-Flow Design for Microfluidic Printing of Two-component Polymer Semiconductor Systems**, *PNAS*, 2020, 117, 17551–17557.

Porous semiconducting films by the breath figure fabrication method. Porous semiconductor film morphologies facilitate fluid diffusion and mass transport into the charge-carrying layers of diverse electronic devices as well as they could provide an avenue to enhance mechanical flexibility and stretchability. In this work, we reported the nature-inspired fabrication of several porous organic semiconductor-insulator blend films [semiconductor: P3HT (p-type polymer), C8BTBT (p-type small-molecule), and N2200 (n-type polymer); insulator: PS] by a breath figure patterning method and their broad and general applicability in organic thin-film transistors (OTFTs), gas sensors, organic electrochemical transistors (OECTs), and chemically doped conducting films. The porous film growth process as exemplified by OTFT fabrication is shown in **Figure 33** along with the dynamics of the film formation and the semiconductors used. Detailed morphological analysis of these films demonstrates formation of textured layers with uniform nanopores reaching the bottom substrate with an unchanged solid-state packing structure. Device data gathered with both porous and dense control semiconductor films demonstrate that the former films are efficient TFT semiconductors but with added advantage of enhanced sensitivity to gases (e.g., 48.2%/ppm for NO₂ using P3HT/PS), faster switching speeds (4.7 s for P3HT/PS OECTs), and more efficient molecular doping (conductivity, 0.13 S/m for N2200/PS) (**Figure 34**).

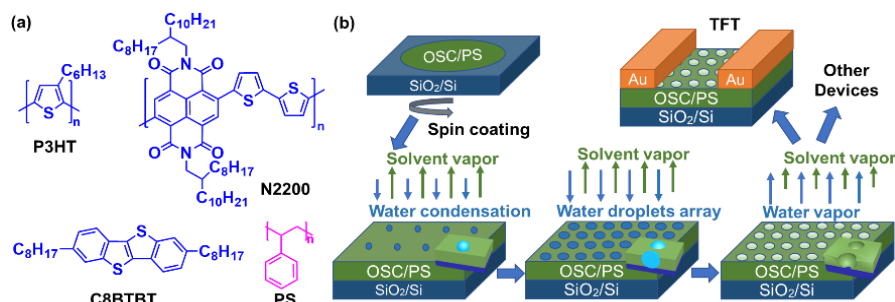


Figure 33. (a) Chemical structures of materials used in this study. (b) Schematic illustration of the porous OTFT structure and the breath figure fabrication process.

Detailed morphological analysis of these films demonstrates formation of textured layers with uniform nanopores reaching the bottom substrate with an unchanged solid-state packing structure. Device data gathered with both porous and dense control semiconductor films demonstrate that the former films are efficient TFT semiconductors but with added advantage of enhanced sensitivity to gases (e.g., 48.2%/ppm for NO₂ using P3HT/PS), faster switching speeds (4.7 s for P3HT/PS OECTs), and more efficient molecular doping (conductivity, 0.13 S/m for N2200/PS) (**Figure 34**).

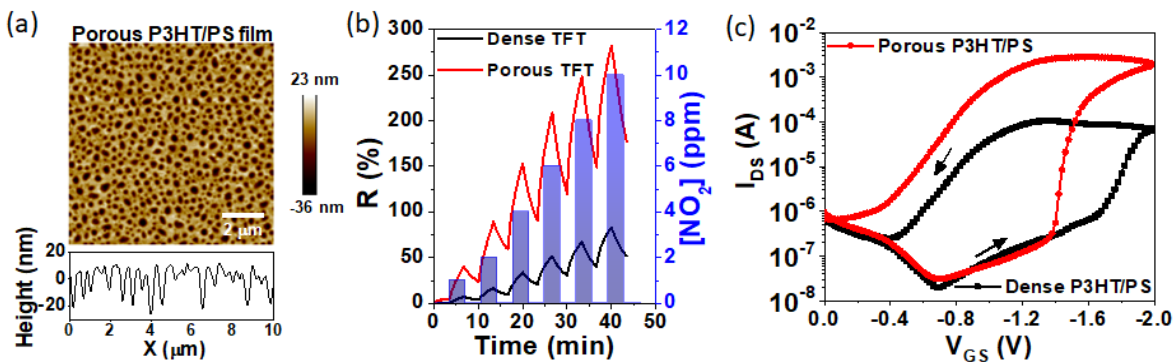


Figure 34. (a) AFM image and the line scan of porous P3HT/PS films. (b) Real-time responsivity ($V_D = V_G = -60$ V) to dynamic NO₂ concentrations (c) Transfer curves of OECTs based on both dense and porous P3HT/PS films.

See: Zhang, X.; Wang, B.; Huang, L.; Huang, W.; Zhu, W.; Wang, Z.; Chen, Y.; Facchetti, A.; Marks, T. J. Breath Figure-Derived Porous Semiconducting Films for Organic Electronics, 2020, *Science Advances*, 2020, 6, eaaz1042. DOI: 10.1126/sciadv.aaz1042.

Mechanically Flexible Semiconductor Films and Devices

Plasticizing grain boundaries of molecular semiconductors. Molecular organic semiconductors have achieved performance greater than those of polymers a result mainly due to the greater extent of degree of texturing of the resulting thin semiconducting films. However, a limitation of molecular semiconductors have is that the substantial thin-film crystallinity and the presence of grain boundaries can compromise charge transport on bending/stretching. One approach we proposed is to synthesize a polymeric binder (PB) that act as plasticizers in the grain boundaries, designed to have a π -conjugated polymeric backbone facilitating transport but that are end-functionalized with units identical to that of the molecular semiconductor of choice (**Figure 35a**). We initiated this study utilizing the n-type molecular semiconductors PDIF-CN₂ considering the availability and good electron transport in rigid substrates and synthesized naphthalenediimide-dithiophene (NDI-T2) polymers end-capped with PDIF-CN units.

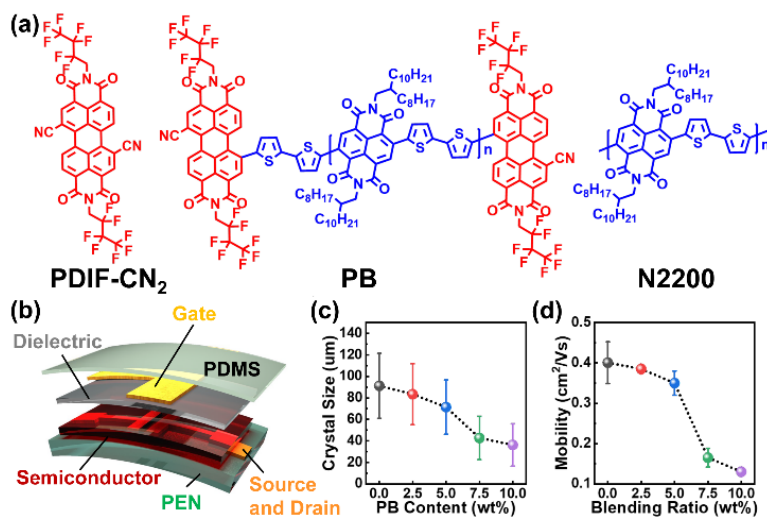


Figure 35. (a) Chemical structures of materials (b) FOTFT structure used. Crystallite (c) size and (d) electron mobility for PB/PDIF-CN₂ blends as a function of PB content.

Note, the hypothesis is that by controlling the polymer backbone architecture, molecular mass (likely at the lower end), and the binder loading in the blend, a balance between thin-film crystallinity, charge transport, and mechanical properties can be found. Thus, the polymeric binder containing end-functionalized PDIF-CN groups have been obtained in good yields and blends investigated (**Figure 35**). The LUMOs of PB and PDIF-CN₂ are properly aligned to favor electron transport. Polycrystalline thin-films of pure PDIF-CN₂ and PDIF-CN₂:PB blends with different weigh ratios were fabricated on flexible PEN substrates (**Figure 36**). The results indicate that the crystalline PDIF-CN₂ films are very rigid and a large number of cracks form after blending the films at as large as a 4 mm radius. Interestingly, when ~5% weight of PB in added to PDIF-CN₂, the crystalline film becomes highly flexible, and maintains a smooth and continuous surface under multiple blending cycles and with bending radii as small as 2 mm (**Figure 36**). Flexible organic TFT (FOTFT) measurements were next conducted in ambient. Thus, pristine PDIF-CN₂ devices (0 wt% PB) exhibit a μ of 0.40 ± 0.05 cm²/Vs with negligible I-

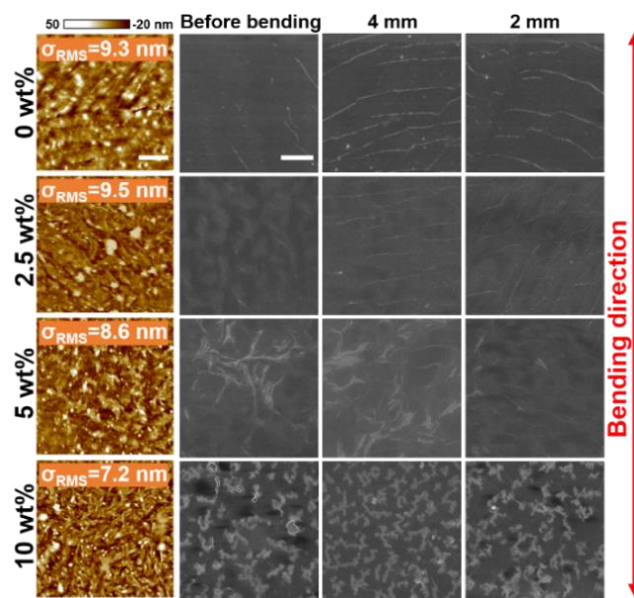


Figure 36. AFM images before deformation (left, scale bar = 4 μ m) and top-view SEM images (right, scale bar = 2 μ m) of PB (x wt%)/PDIF-CN₂ before and after bending at the indicated radii.

V hysteresis. As the PB content increases from 2.5 wt% to 10 wt%, both the I_{on} and I_{off} currents first fall minimally (2.5-5%) and then substantially. Thus, the electron mobility decreases from 0.38 ± 0.01 (2.5 wt%) \rightarrow 0.35 ± 0.05 (5 wt%) \rightarrow 0.16 ± 0.03 (7.5 wt%), and finally to 0.13 ± 0.02 cm^2/Vs (10 wt%). This mobility decline likely reflects reduction of crystallite size, hence increased grain boundary densities, rather than PB presence since a similar trend was seen for TFTs based on vapor-deposited PDIF-CN₂ films fabricated at progressively lower temperatures, which reduces the crystal domain size.

Next, we evaluated charge transport behavior after the FOTFTs were deformed by bending at a radius from ∞ (no extensional stress) to 2 mm (stress \sim 3%) parallel to the charge transport direction (along the channel length, L). From **Figure 37**, the μ variation upon bending strongly depends on the semiconductor composition with the TFTs with the 5 wt% blend exhibit the best compromise between initial performance ($\mu = 0.35 \pm 0.05$ cm^2/Vs) and mobility degradation after 2 mm bending ($\mu = 0.22 \pm 0.03$ cm^2/Vs). The 5 wt% blend exhibits negligible variations of other TFT parameters such as threshold voltage and current on-off

ratio, as well as no substantial changes in transport when measured in the 2 mm bended state versus after bending at 2 mm. Repeated bending tests were performed on all devices at 4 mm for 500 cycles confirming that the 5wt% TFT blend affords the best compromise between initial and final performance. More importantly, the mobility of the N2200 + PDIF-CN₂ FOTFTs bent at a 4 mm radius for 500 cycles decreases by \sim 90% (from 0.55 to 0.06 cm^2/Vs). Together these results demonstrate that N2200 alone cannot increase PDIF-CN₂ film flexibility.

Since PB addition to PDIF-CN₂ clearly enhances film mechanical properties, the question of how PB creates a more elastic morphology and whether this reflects a specific PB special distribution within the crystalline domains, arises (**Figure 38**). SEM images show that increasing the blend PB content, particularly beyond 5 wt%, creates brighter features along the film grain boundaries, suggesting preferential PB localization at the crystallite edges. To better

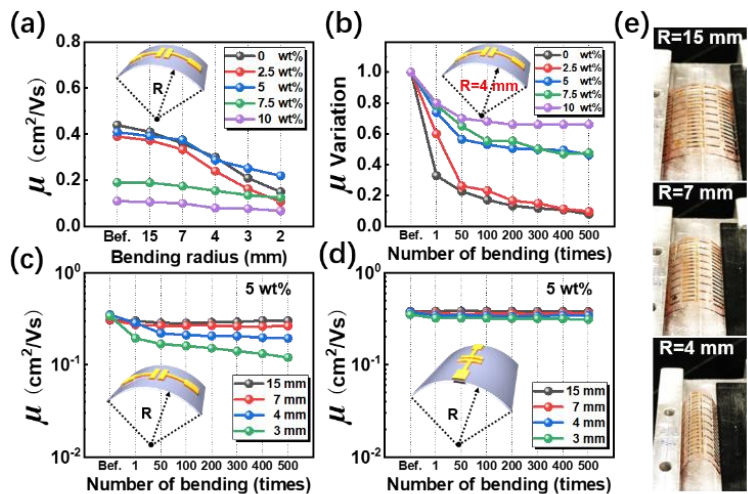


Figure 37. Electron mobility variations of PB (x wt%)/PDIF-CN₂ FOTFTs (x = 0-10) upon deformation at (a) different bending radii and (b) for different bending cycles. Electron mobility of PB (5 wt%):PDIF-CN₂ FOTFTs upon bending deformation at different radii (c) along the L channel direction and (d) perpendicular to the L direction. (e) Optical images of bended FOTFTs before testing.

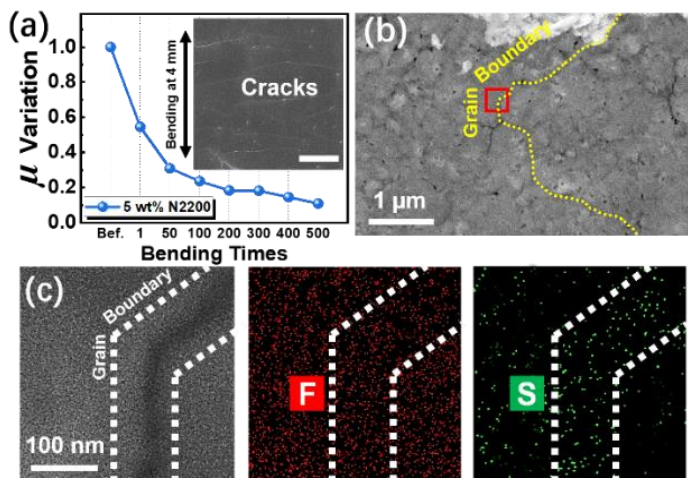


Figure 38. (a) μ variation of N2200(5 wt%)/PDIF-CN₂ FOTFTs upon varied bending cycles ($R = 4$ mm). Inset SEM image after the first bending at $R = 4$ mm (scale bar = 2 μm). (b) STEM image and (c) Magnification and EDS elemental maps [Fluorine (red) and Sulfur (green)] for the indicated area in (b) for the PB(5 wt%)/PDIF-CN₂ blend.

understand this, STEM-EDS mapping of the 5 wt% blend was carried out. By mapping the F (PDIF-CN₂ and PB end groups) and S (PB only) distributions, PB mainly accumulates at the PDIF-CN₂ grain boundaries.

See: Zhao, D.; Chen, J.; Wang, B.; Wang, G.; Chen, Z.; Yu, J.; Guo, X.; Huang, W.; Marks, T. J.; Facchetti, A., Engineering Intrinsic Flexibility in Polycrystalline Molecular Semiconductor Films by Grain Boundary Plasticization *J. Am Chem Soc* 2020, 142, 5487.

Mechanically flexible polymers using deconjugated subunits. Another approach in our semiconductor development originates in our recent discovery that by manipulating the molecular orbital topologies of the key semiconducting polymer building block and degree of backbone π -conjugation in a class of n-type naphthalene-diimide-based

polymers (PNDI-TV_Tx, **Figure 39**), it is possible to greatly soften the polymers with only slight decline in the charge transport characteristics. For example, on going from fully conjugated PNDI-TV_T100 to the polymer where the conjugation is greatly reduced by inserting ~60% of the deconjugated TET block (PNDI-TV_T40), the electron mobility is essentially unchanged, but there is a considerable improvement in solution processability of these polymers, and a strong depression in the melting point (from 273 to 226 °C). Note, however, that the hole mobility in these polymers (enabled using specialized gate dielectrics) strongly declines. This result is explained by substantial localization of the PNDI-TV_T100 LUMO in the NDI units, which is minimally affected by disrupting the in-chain π -conjugation, while in contrast, the PNDI-TV_T100 HOMO is more delocalized on the backbone, resulting a far larger dependence of the hole mobility on the backbone π -conjugation.

In recent experiments we have seen that the softening of the PNDI-TV_Tx films as assessed by the

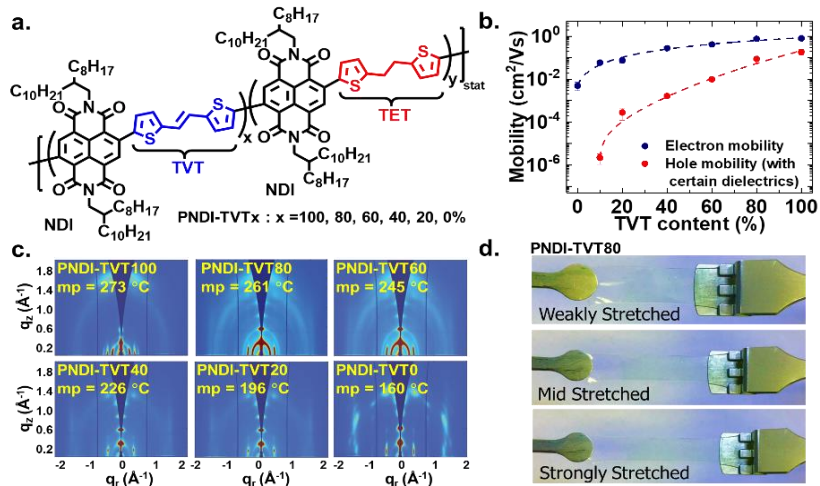


Figure 39. a. Chemical structure of PNDI-TV_Tx polymers b. TFT mobilities of PNDI-TV_Tx as a function of the x content. Note, hole transport is observed only using certain dielectrics. c. Film microstructure by GIWAXS and melting temperature by DSC for the indicated PNDI-TV_Tx polymers. d. Optical images of a free-standing PNDI-TV_T80 films stretched to varying degrees.

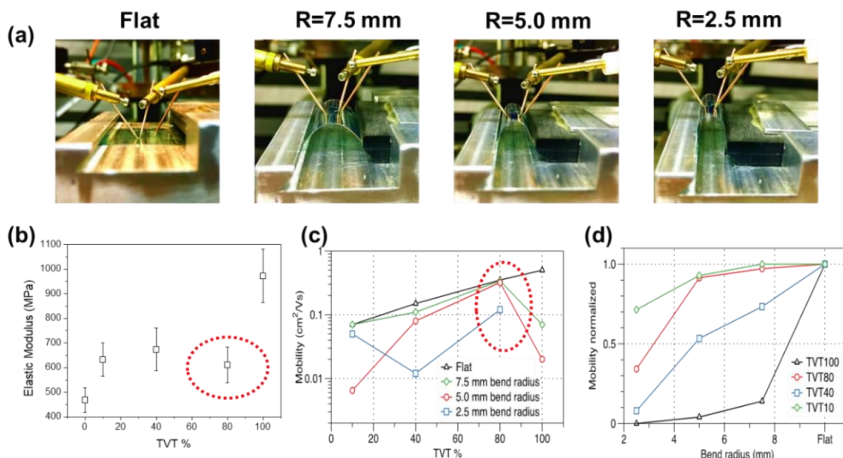


Figure 40. Evaluation of mechanical and electronic properties of PNDI-TV_Tx polymers. (a) Photographs of fabricated flexible transistors at various bend radii; (b) Elastic modulus of PNDI-TV_Tx at various conjugation concentrations; (c) Plots of mobility vs conjugation concentration; and (d) Plots of mobility vs bend radius.

melting point translate to elastic modulus reduction from ~ 1 GPa for PNDI-TVT100 to ~ 0.4 GPa for PNDI-TVT80 and, more importantly, a reduction of the mobility sensitivity with mechanical stress. Thus, when PNDI-TVTx TFTs are bent from $R = \infty \rightarrow 0.5 \rightarrow 0.25$ mm the electron mobility drops from $\sim 0.5 \rightarrow 0.02 \rightarrow <10^{-5}$ cm^2/Vs for PNDI-TVT100 whereas only $\sim 0.35 \rightarrow 0.32 \rightarrow 0.12$ cm^2/Vs for PNDI-TVT80, with the softer polymer exhibiting significantly lower sensitivity (**Figure 40**). We recently acquired detailed GIWAXS (grazing-incidence wide angle X-ray scattering) data while stretching the polymers with and without the polymeric dielectric layer to understand change in semiconductor film microstructure. The analysis of these results is in progress. We also investigated how doping and deconjugation affect the mechanical properties of these polymers (**Figure 41**). Very interestingly, the conductivity data reflect the FET mobility trends corroborating that the deconjugation strategy extends to high carrier density regimes.

In parallel, we investigated the influence of backbone regiochemistry on the conductivity, charge density, polaron structure, and mechanical flexibility of N2200. In contrast to classic semicrystalline polymers such as poly(3-hexylthiophene) (P3HT), the regioirregular (RI) linkage between the naphthalenediimide (NDI) and the bithiophene (T2) units in N2200 does not vary the intramolecular steric demand of the backbone versus the regioregular (RR) isomer, allowing the RI polymer to exhibit similar LUMO energy and optical features as its RR counterpart (**Figure 42**). By combining electrical, UV-Vis/IR, X-ray diffraction, epr data and DFT calculations,

we quantitatively characterized the conductivity, aggregation, crystallinity, charge density and simulated the polaron structures, molecular vibrations and spin-density distribution of RR-/RI-P(NDI2OD-T2). Importantly, we observed that RI-P(NDI2OD-T2) can be doped to a greater extent compared to its RR counterpart (**Figure 43**). This finding is remarkable and contrasts benchmark P3HT. This unique feature provides us with an ideal testbed to separately study the role of textural order along the different crystallographic axes on the charge transport properties of n-doped donor-acceptor polymers.

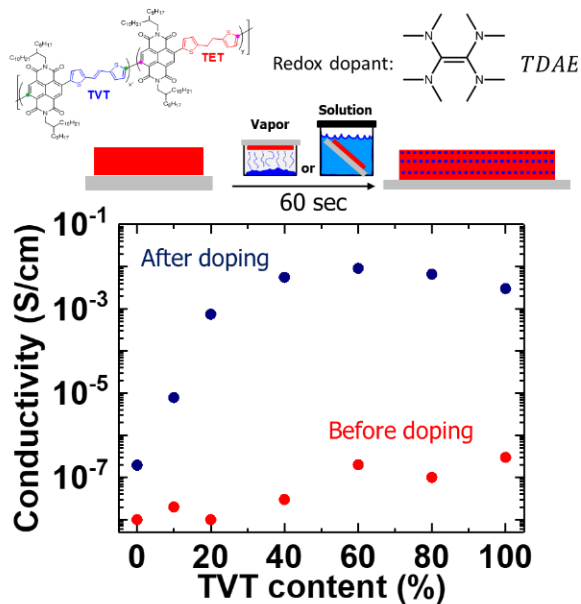


Figure 41. Conductivity evolution as a function of the deconjugated unit content.

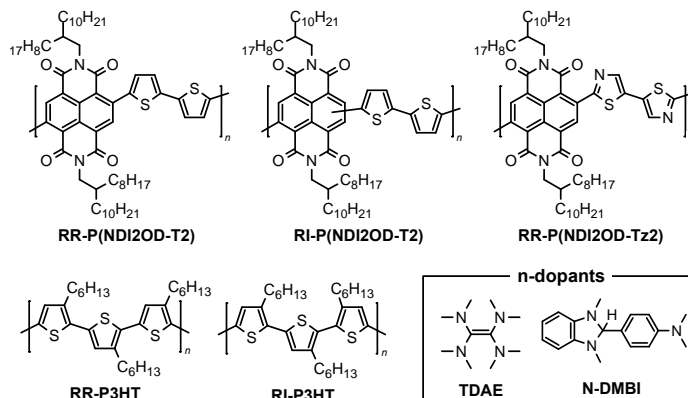


Figure 42. Chemical structures of typical donor-acceptor polymers such as RR-P(NDI2OD-T2) (N2200), RI-P(NDI2OD-T2), RR-P(NDI2OD-Tz2), as well as RR-P3HT and RI-P3HT. Chemical structures of typical n-dopants used in this study

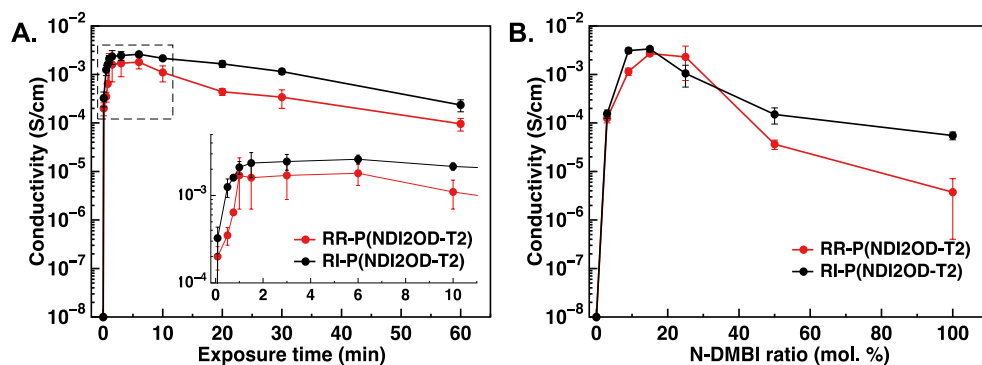


Figure 43. Conductivity evolution as a function of the deconjugated unit content. Electrical conductivity of RR- and RI-P(NDI2OD-T2) bulk films as a function of a) TDAE exposure time, and b) N-DMBI molar ratio.

See: Wang, S.; Fazzi, D.; Puttison, Y.; Jafari, M. J.; Chen, Z.; Ederth, T.; Andreasen, J. W.; Chen, W. M.; Facchetti, A.; Fabiano, S. Effect of Backbone Regiochemistry on Conductivity, Charge Density, and Polaron Structure of n-Doped Donor-Acceptor Polymers. *Chem. Mater.* **2019**, *31*, 3395-3406.

Mechanically flexible polymer films achieved by porosity. Organic electrochemical transistors (OECTs), a type of organic transistor where mixed electronic-ionic charge transport occurs, have attracted numerous research attentions due to their intrinsic merits including low driving voltage, sensitive ion detection and excellence in small signal amplification (*vide infra*, **Figure 44d**). However, previous studies on OECTs were mostly fabricated on rigid substrates and suffer from stability issues, which could be problematic when integrate with biological tissues (e.g., human skin), where excellent flexibility, even stretchability and stable performance of the OECTs are required for reliable signal generation/receiving.

Here we report ultra-stretchable and electrochemically redox-stable OECTs with negligible performance degradation under tensional strains both parallel and perpendicular to channel length directions up to 30-140%, depending on the platform and limited only by metal contact fatigue. This unprecedented result is realized by combining a novel amphiphilic semiconducting polymer which achieves a uniform honeycomb film morphology, poly(2,5-bis(2-octyldecyl)-3,6-di(thiophen-2-yl)-2,5-diketo-pyrrolopyrrole-alt-2,5-bis(3-triethyleneglycoloxy-thiophen-2-yl) (DPP-g2T), with a biaxially pre-stretched film/device architecture. These factors stabilize the effective electronic and ion transport pathways under deformation, leading to OECTs with a high normalized transconductance and stable output characteristics upon deformation. For this objective we designed and synthesized a new polymer, DPP-g2T (**Figure 44a**). DPP-g2T was selected as the candidate for this study based on experiments with the counterpart polymer DPP-2T without ethylene glycol side chains (**Figure 44a**). Cyclic voltammetry (CV) of DPP-g2T and DPP-2T reveal oxidation onsets at +0.34 and +0.75 V, respectively, and that DPP-g2T is more readily oxidized. The spectro-electrochemical properties of DPP-g2T and control DPP-2T films on ITO/glass were characterized under biases ranging from 0.0 V to +0.8 V (in 0.1 M KPF₆) to investigate the electrochemical doping efficiency. For DPP-g2T, upon application of a low bias the intensities of the π - π^* absorption (420 nm), intramolecular charge transfer (ICT, 783 nm), and π - π aggregate (848 nm) peaks decrease and polaronic absorption at longer wavelengths (> 1000 nm) increases, indicating full and efficient doping of DPP-g2T. In contrast, the DPP-2T film shows no obvious absorption changes at biases \leq +0.5 V and even at a biases \geq +0.8 V, while the absorption features of the neutral polymer persist, indicating poor electrochemical doping efficiency. In addition, the absorption spectrum of DPP-g2T returns to the original line shape when applying a bias of -0.2 V, while that of DPP-2T only partially recovers, indicating inferior redox stability,

a result confirmed by CV measurements on the same platform (**Figure. 44b**). The overall results indicate that DPP-g2T is more readily oxidized and that the electrochemical process is quantitatively more efficient and far more stable than that of DPP-2T. Consequently, addition of the ethylene glycol side chain not only enables stable electrochemical properties but also facilitates the ion uptake from aqueous electrolytes due to its hydrophilicity, cationic chelating ability, and favoring ion exchange.

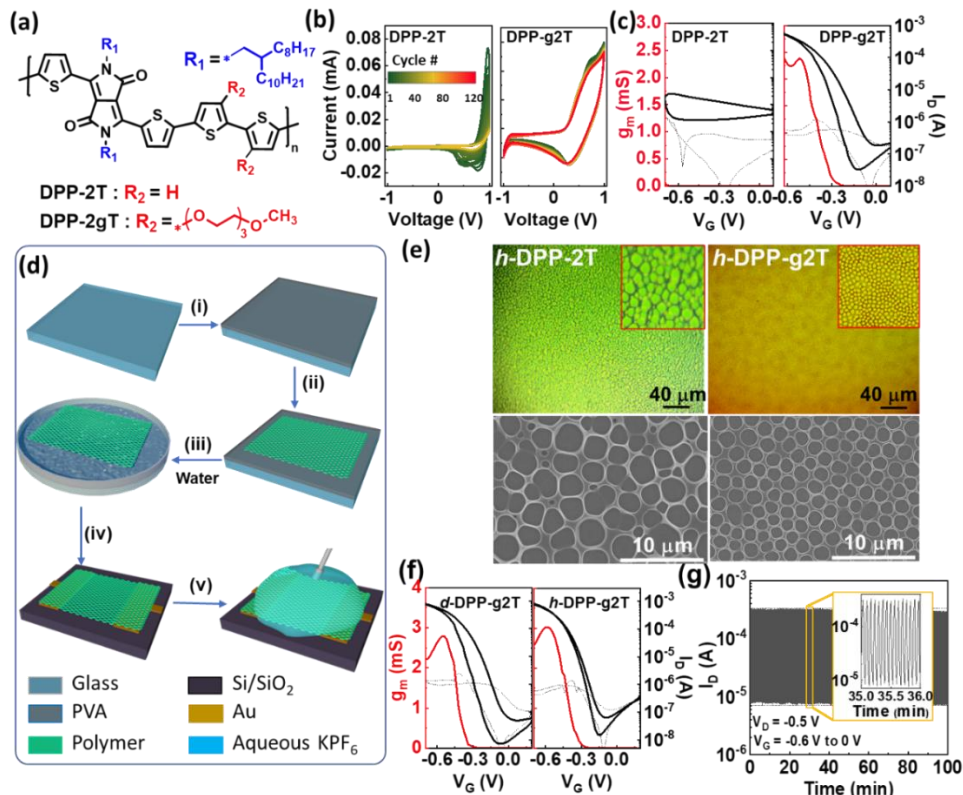


Figure 44. (a) Molecular structures of polymers DPP-2T and DPP-g2T. (b) Cyclic voltammetry of DPP-2T and DPP-g2T films on ITO/glass substrates. (c) Transfer and transconductance plots of OEECTs ($W/L = 600 \mu\text{m}/25 \mu\text{m}$, $V_D = -0.5\text{V}$) based on spin-coated dense(*d*)-DPP-2T (56 nm) and *d*-DPP-g2T (65 nm) films. The dash lines represent the gate current. (d) Schematic of OEECT fabrication process using honeycomb films (e) Optical (top) and SEM (bottom) images of *h*-DPP-2T (left) and *h*-DPP-g2T (right) films. The insertion shows a zoom-in of the images. (f) g_m and I_b vs. V_g plots of OEECTs ($W/L = 600 \mu\text{m}/25 \mu\text{m}$, $V_D = -0.5\text{V}$) based on transferred *d*-DPP-g2T (78 nm) and *h*-DPP-g2T (50 nm) films. The dash lines represent the gate current. (g) Transient characteristics of *h*-DPP-g2T-based OEECT on a Si/Au substrate by applying alternating gate potentials of $V_g = -0.6 \text{V}$ and 0.0V with $V_D = -0.5 \text{V}$ and a pulse duration of 2 s for 100 min.

OEECT performance for both DPP-2T and DPP-g2T was first investigated by fabricating rigid OEECTs of structure Si/300 nm SiO₂ (substrate)/Au (source-drain contacts)/ polymer film (semiconductor)/0.1 M KPF₆ (electrolyte)/Ag-AgCl (gate) with a channel width (W)/length (L) of 600 μm/25 μm. For these devices the polymer films were deposited by a conventional spin-coating protocol that affords dense, continuous films. The transfer, transconductance, and output curves (**Figure. 44c**) indicate that both polymers are p-channel semiconductors and function in accumulation mode. Clearly the DPP-g2T OEECTs turn-ON far more readily than those fabricated from DPP-2T, and the two exhibit $V_T = -0.28 \text{V}$ and -0.59V , respectively. The average maximum transconductance (g_m) of the DPP-g2T OEECTs is $2.47 \pm 0.24 \text{mS}$ at $V_G = -0.51 \text{V}$ while that of the DPP-2T devices is $0.064 \pm 0.016 \text{mS}$ recorded at $V_G = -0.70 \text{V}$. Since the OEECT performance is determined by both channel materials properties and channel geometry, a normalized peak g_m ($g_{m,n}$) is

calculated by $g_{m,n} = \frac{L}{wd} g_m$, where d is the semiconductor thickness, resulting in a $g_{m,n}$ of 15.83 ± 1.54 S/cm and 0.26 ± 0.07 S/cm for DPP-g2T and DPP-2T, respectively. In addition, note that the hysteresis for DPP-g2T (63 mV) is significantly lower compared to DPP-2T (383 mV). This OECT performance analysis clearly demonstrates that DPP-g2T outperforms DPP-2T, in agreement with the aforementioned CV and spectro-electrochemical data.

In recent work we reported the fabrication of porous organic semiconductor films by a breath figure technique for applications in sensors, doping, and OECTs. However, only limited control of the porous film architecture was achieved. Here, by implementing the DPP-g2T backbone functionalized with amphiphilic substituents, using a hydrophilic sacrificial layer on the substrate, and precise heat transfer control during/after the film spin-coating, uniform porous honeycomb DPP-g2T structures over large areas are achieved (**Figure. 44e**). This film and subsequent OECT fabrication are shown in **Figure. 44d**. Note, for hydrophobic DPP-2T, porous films can be obtained but with randomly distributed pore patterns (**Figure. 44e**). Both h - and d -films were transferred to Si wafer substrates to first investigate film morphology. Thus, the optical, AFM and SEM images (**Figure. 44e**) reveal that all transferred d -films are relatively smooth while the h -DPP-g2T exhibits a uniform honeycomb structure with an average pore diameter of 1.33 ± 0.15 μm and wall height of 183 ± 34 nm. In contrast, h -DPP-2T films exhibit very non-uniform craters of diameters ranging from $1.3 \sim 3.6$ μm (average = 2.14 ± 0.83 μm) and wall height of 322 ± 86 nm. OECTs based on the h - and d -films of both polymers were fabricated on Au (source-drain)/Si substrates to assess how the film morphology affects, *vis-à-vis* the polymer structure, charge transport (**Figure. 44d**). The OECT data indicate that DPP-g2T OECTs outperform DPP-2T OECTs and, most importantly, that the h -films of both polymers outperform those of the corresponding d -films in OECTs. Thus, the $g_{m,n}$ of h -DPP-g2T is $\sim 2x$ that of d -DPP-g2T and the former devices exhibit negligible hysteresis vs the latter (~ 20 mV vs. ~ 100 mV) due to fast ion exchange benefited from efficient electrolyte-semiconductor interfacial area of h -DPP-g2T. Furthermore, h -DPP-g2T shows slightly lower V_T (-0.31 V vs. -0.34 V) than d -DPP-g2T (**Figure. 44f**). Transient OECT characteristics measured by switching V_G between -0.6 V and 0.0 V ($V_D = -0.5$ V, 2 s pulses over 100 min) were also carried out to probe the stability of the d - and h -DPP-g2T OECTs and reveal negligible current degradation after 1500 redox cycles, placing them among the most stable OECTs reported to date. These combined results demonstrate the great advantage of a specifically designed semiconducting polymer microstructure having a honeycomb OECT channel morphology for optimal charge transport.

It is well known for metals and other electronic materials that proper morphology implementation (serpentine, raised wave, fibrous) can greatly enhance mechanical properties including flexibility. Based on these motivations, uniform honeycomb structures should be more stretchable than continuous films owing to the possibility of pore deformation. To investigate this hypothesis, finite element analysis (FEA) simulations were carried out for free-standing d - and h -films. These indicate that h -films should sustain larger strain ($+ \sim 50\%$) before cracking than the d -films (**Figure. 45a**) because the out-of-plane buckling deformation of the thin h -films facilitates geometric expansion of the honeycomb structure and releases local stress concentrations during stretching. Thus, film-on-elastomer tensional strain measurements were carried out for the porous h - and d -films transferred to SEBS substrates. Interestingly, the tensile stress experiments (**Figure. 45b**) indicate that d -/ h -DPP-2T films crack at a lower strain (ϵ , 110/60%) than the corresponding d -/ h -DPP-g2T films (ϵ , 160/130%), with the latter among the largest to date for fully π -conjugated polymers, and further supporting the rationale of choosing DPP-g2T for fabricating stretchable devices (*vide infra*). However, in contrast to the FEA results on free-standing films, both h -films crack earlier than the corresponding dense ones. To understand this result, additional FEA simulations using film-on-elastomer platforms were performed (**Figure. 45c**). The simulation results show that the stretchability of the h -films decrease as the modulus of the substrate increases while that of the d -films are independent.

This is because as the Young's modulus of the elastomeric substrate increases, the in-plane deformations of the *h*-film dominates over out-of-plane buckling and enhances local stress. Thus, since the SEBS substrates use in our work had a Young's modulus of 5.2 MPa, the film-on-elastomer results fall in the modulus region of the **Figure. 45c** plot where the *h*-films are expected to crack first, explaining the experimental results.

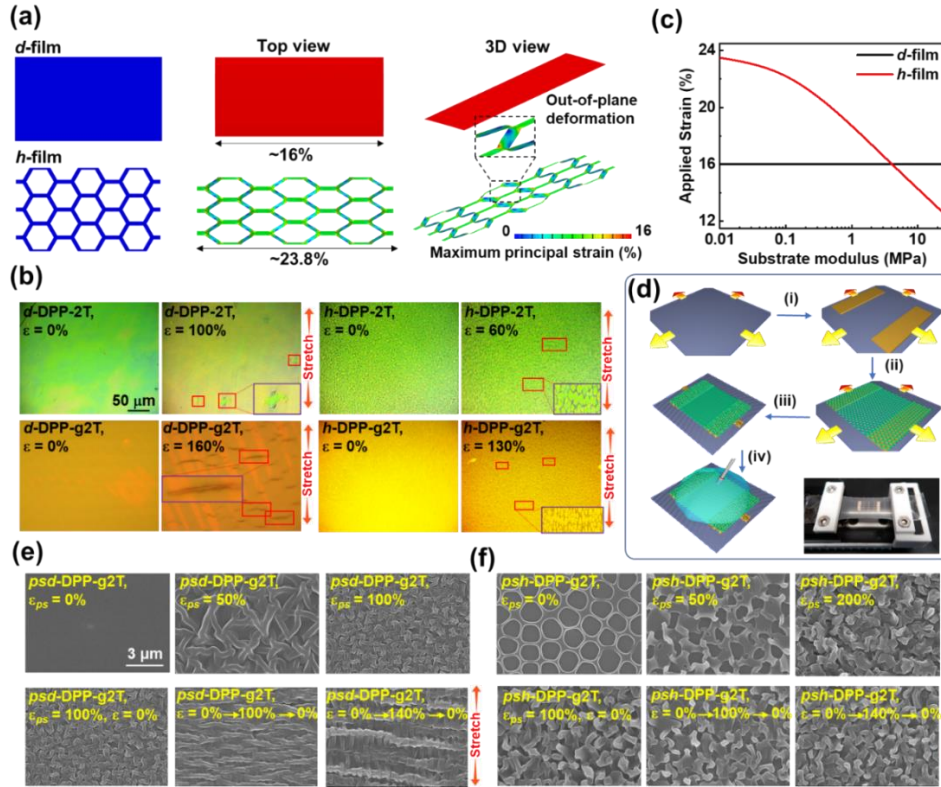


Figure 45. (a) Finite element analysis (FEA) of freestanding *d*- and *h*-films. (b) Tensile stress results of *d*-/*h*-DPP-2T and DPP-g2T films. (c) FEA simulation for film-on-elastomer platforms. (d) Illustrations of pre-stretched OECT (*ps*-OECT) fabrication process. (e) SEM images of *psd*-DPP-g2T films originating from SEBS substrate pre-stretched (*ps*) at a strain of $\epsilon_{ps} = 0\%$ (no *ps*), 50%, and 100% after releasing the strain (top images) while bottom images correspond to 100% *ps*-film stretched to different strains and returned to the relaxed state ($\epsilon = 0 \rightarrow 100 \rightarrow 0\%$ and $0 \rightarrow 140 \rightarrow 0\%$). (f) SEM images of *psh*-DPP-g2T films originating from SEBS substrates pre-stretched (*ps*) at a strain of $\epsilon_{ps} = 0\%$ (no *ps*), 50%, and 200% after releasing the strain (top images) while bottom images correspond to a 100% *ps*-film stretched to different strains and returned to relaxed state ($\epsilon = 0 \rightarrow 100 \rightarrow 0\%$ and $0 \rightarrow 140 \rightarrow 0\%$).

Based on the results of the mechanical properties, OECTs employing transferred *d*- and *h*-DPP-g2T films on SEBS substrates should be stretchable up to 160/130%. However, we found that these devices are poorly stretchable and performance deteriorates at $\epsilon \sim 20\%$, a result dominated by cracks forming at the electrodes, reflecting the poor stretchability of Au films on elastomers. Therefore, to retain Au as electrical contact, device stretchability was enhanced by biaxially pre-stretching the SEBS substrate prior to Au deposition and semiconductor film transfer (**Figure. 45d**). This is a well-known procedure to enhance the mechanical robustness of metal contacts. Before electrical evaluations, the morphology of the *d*- and *h*-DPP-g2T films on the biaxially pre-stretched (*ps*) SEBS substrates was investigated after releasing the biaxial strain, hereafter indicated as *psd*- and *psh*-films/OECTs, since the use of *h*-films plays a key role in this study (*vide infra*). SEM images of these films on various SEBS substrates pre-stretched at different strains ($\epsilon_{ps} = 0\%$, 50%, 100%, 150%, and 200% (**Figure. 45e,f**) show that the *psd*-films fold/collapse at a $\epsilon_{ps} \sim 50\%$ while for *psh*-films this phenomenon occurs above $\epsilon_{ps} \sim 150\%$. Furthermore, advancing aqueous contact angle measurements indicate that the pre-stretched dense films are more hydrophobic, thus less macroscopically

prone to wetting by the aqueous electrolyte solution. Therefore, adoption of a honeycomb structure is crucial when utilizing a pre-stretch strategy, since contacting the semiconductor film with the electrolyte remains very effective. Tensile stress experiments on the 100% pre-stretch *psd*- and *psh*-films ($\epsilon_{ps}=100\%$; $\epsilon = 20\% \rightarrow 200\%$) shows that both films can be stretched to a remarkable 200% without evident cracking. However, only the *psh*-DPP-g2T films retain the same morphology after releasing the strain since the *psd*-DPP-g2T films evidence severe wrinkling perpendicular to the strain directions (**Figure. 45e,f**). Indeed, on increasing the tensile strain from 20% to 100%, the compressed pores begin to gradually unfold, with the bended walls straightening in the strain direction. Thus, deformation of the *psh*-DPP-g2T films in fact relies on honeycomb wall bending to deform, other than directly stretching.

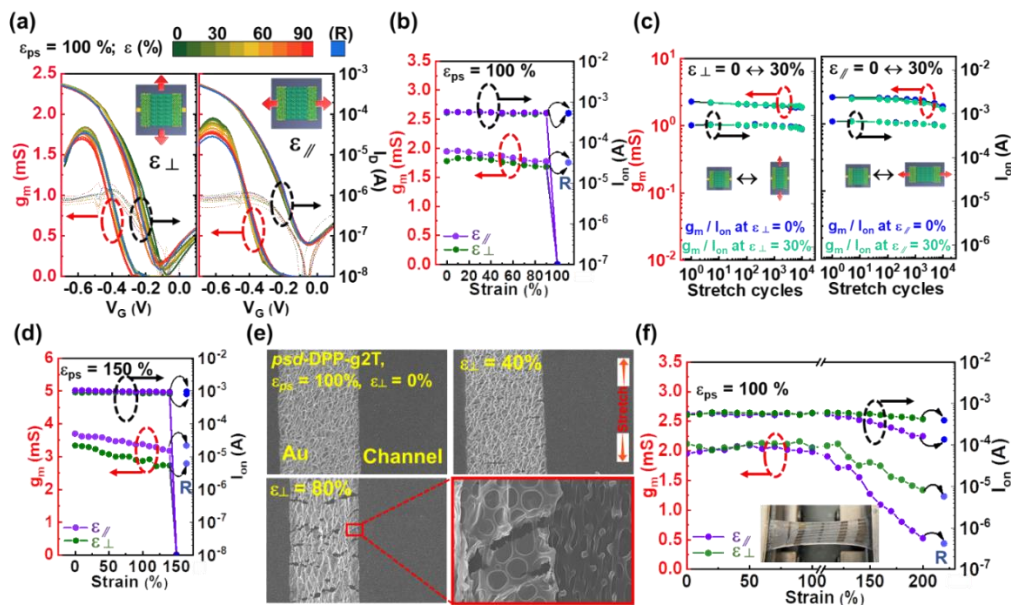


Figure 46. (a) Transfer and transconductance plots and (b) g_m / I_{on} data for *psh*-DPP-2gT ($\epsilon_{ps}=100\%$) OECTs under various strains perpendicular (ϵ_{\perp}) or parallel (ϵ_{\parallel}) to channel length directions. R = strain was relaxed to 0%. (c) g_m dependence on stretching cycles for *psh*-DPP-2gT ($\epsilon_{ps}=100\%$) OECTs in ϵ_{\perp} or ϵ_{\parallel} directions, where g_m s under 0% and 30% elongation strains are recorded. (d) g_m / I_{on} for *psh*-DPP-2gT ($\epsilon_{ps}=150\%$) OECTs under various strains (from 0% to 150%) in ϵ_{\perp} or ϵ_{\parallel} direction. (e) SEM images for a *psh*-DPP-2gT ($\epsilon_{ps}=100\%$) under 0%, 40%, and 80% strains. Note significant Au line rupture when the *h*-film remains connected. (f) g_m / I_{on} for *psh*-DPP-2gT ($\epsilon_{ps}=100\%$) OECTs based on Ecoflex/SEBS bilayer substrates under various strains (from 0% to 200%) in ϵ_{\perp} or ϵ_{\parallel} direction.

OECTs using *psd*- and *psh*-DPP-g2T were first fabricated by transferring the *d*-/*h*- free-standing semiconducting polymer films onto 100% pre-stretched SEBS substrates ($\epsilon_{ps}=100\%$) having transferred Au source/drain electrodes and were evaluated with tensional strains applied along directions parallel (ϵ_{\parallel}) or perpendicular (ϵ_{\perp}) to L (**Figure. 46a, b**). Notably, the *psd*-DPP-g2T OECTs before deformation (ϵ_{\parallel} and $\epsilon_{\perp}=0\%$) exhibit a $I_D=4.08\pm 0.21\times 10^{-4}$ A, a $V_T=-0.44$ V, and $g_m/g_{m,n} = 2.44\pm 0.13$ mS / 13.03 ± 0.69 S/cm (Table 1, Entry 9) while the *psh*-DPP-g2T devices yield $I_D = 5.37\pm 0.15\times 10^{-4}$ A, $V_T = -0.28$ V, and $g_m / g_{m,n} = 1.94\pm 0.03$ mS / 16.16 ± 0.25 S/cm. Besides the lower current, the *psd*-DPP-g2T OECTs exhibit very large hysteresis (~ 300 mV) vs the *psh*-DPP-g2T devices (< 40 mV). Upon stretching these devices to ϵ_{\parallel} and $\epsilon_{\perp} = 90\%$, the *psh*-DPP-g2T devices exhibit stable transfer characteristics, with only minor variations in both drain current (I_D) and g_m [$\sim 10\%$] with strain. In contrast, the best *psd*-DPP-g2T OECTs respond very differently with the peak g_m s gradually falling to 78% and 56% of the initial values when ϵ_{\parallel} and ϵ_{\perp} of 90%, respectively, are applied. These results indicate that the *psh*-film morphology is ideal for stretchable OECTs, enabling excellent both mechanical stretchability and stable electrical response under stretching.

For on-skin bioelectronic applications, OECT performance should be insensitive over the range of maximum strain tolerated by human skin ($\sim 30\%$). Thus, *psh*-DPP-g2T ($\epsilon_{ps}=100\%$) OECT performance was monitored over stretching cycles ($\epsilon_{//}$ or $\epsilon_{\perp}=0\leftrightarrow 30\%$) and evidenced excellent mechanical robustness with maximum g_m degradation of 13% or 8% after 1000 stretching cycles and $\sim 27\%$ or 20% after 10000 stretching cycles, respectively (**Figure. 46c**). Even higher stretchability can be achieved by applying a larger pre-stretching to the SEBS substrate --for example the *psh*-DPP-g2T OECTs ($\epsilon_{ps}=150\%$) can be stretched to $\epsilon_{//}$ or $\epsilon_{\perp}=140\%$ with 90% or 83% g_m retention (**Figure. 46d**). Note, all pre-stretched DPP-g2T devices at $\epsilon_{ps}=100\%$ or 150% exhibit, independent of the semiconductor film morphology, catastrophic failure at $\epsilon_{//}\approx \epsilon_{\perp}$ of 100% or 150%, respectively. The small performance degradation in all devices for $\epsilon_{//}\approx \epsilon_{\perp} < \epsilon_{ps}$ and failure for $\epsilon_{//}\approx \epsilon_{\perp} \geq \epsilon_{ps}$ originate from microcracks and eventual complete Au electrode rupture/delamination, respectively (**Figure. 46e**). Finally, as proof-of-concept, stretchability can be enhanced further, and parameters greatly stabilized for $\epsilon_{//}\approx \epsilon_{\perp} > \epsilon_{ps}$, by thermally evaporating Au contacts directly on pre-stretched Ecoflex/SEBS substrates instead of stamping (**Figure. 46f**).

The above results indicate that DPP-g2T OECT charge transport is insensitive to mechanical deformations, in marked contrast to most previously reported stretchable transistors. Stable electrical performance is critical in a great many applications where consistent signal output is essential under deformation. For instance, epidermal electronics and electronic joints of biomimetic robotics demand device performance that is immune to mechanical deformations. To probe the reliability of the present OECTs under these application scenarios, we measured electrocardiogram (ECG) and simulated synapse characteristics when the present OECTs were subjected to various strains, demonstrating excellent response (**Figure. 47**).

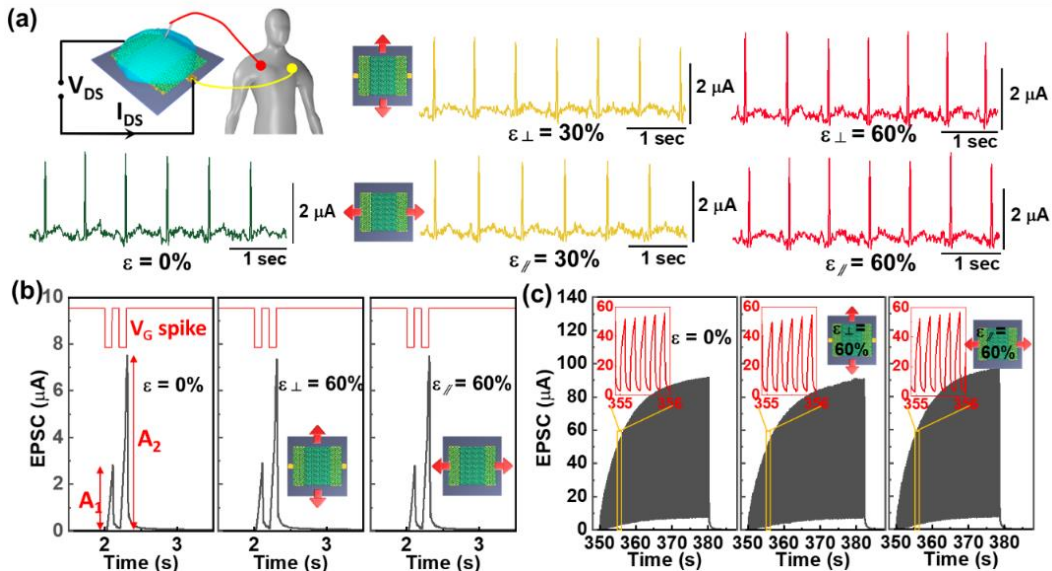


Figure 47. (a) Illustration of electrocardiogram (ECG) recording set-up and spontaneous heart activity measured on a human volunteer with the *psh*-DPP-2gT OECT ($\epsilon_{ps}=100\%$; aqueous KPF₆ electrolyte) under different elongation strains (0%, 30% and 60%) in the ϵ_{\perp} or $\epsilon_{//}$ direction. (b-f) Synaptic characteristics of *psh*-DPP-2gT ($\epsilon_{ps}=100\%$) OECT under 0%, and 60% elongation strains in ϵ_{\perp} or $\epsilon_{//}$ direction. Excitatory postsynaptic current (EPSCs) triggered by (b) double spikes and (c) multiple spikes (each spike: -0.7 V, 100 ms; interval: 100 ms). A₁ and A₂ are EPSCs of the first and second spikes, respectively.

See: Chen, J.; Huang, W.; Xie, Z.; Zhuang, X.; Zhao, D.; Chen, Y.; Su, N.; Chen, H.; Pankow, R.M.; Gao, Z.; Yu, J.; Guo, X.; Yu, X.; Marks, T.J.; Facchetti, A.; Ultra-Stretchable Organic Electrochemical Transistors with Strain-Resistant Performance, *Nature Materials*, revised

New Organic Transistor Architectures

As discussed above, OEETs are attractive for bioelectronics, wearable electronics, and artificial neuromorphic electronics, because of their low driving voltage, high transconductance, and facile integration in mechanically flexible platforms. However, further OEET development faces several challenges: *i*) Poor electron-transporting (n-type) OEET performance ($\sim 1000\times$ lower transconductance/current density and inferior stability) versus their hole-transporting (p-type) counterparts (8-10). *ii*) Unbalanced p-type and n-type OEET performance prevents efficient integration into complementary circuits. *iii*) Poor n-type OEET performance leads to inferior sensitivity to *in vivo* relevant analyte cations (e.g., Na^+ , K^+ , Mg^{2+} , Ca^{2+} , Fe^{3+} , Cu^{2+} and Zn^{2+}) severely hindering development of OEET biosensors (2). *iv*) The best performing conventional OEETs (cOEETs), having planar source/drain electrode architectures, require small channel lengths (L) of $\leq 10 \mu\text{m}$, along with a precisely-patterned semiconducting layer and covering of the electrodes with passive materials, to yield high transconductance (g_m) and fast switching ($\sim \text{ms}$ range) devices. This requires complex fabrication methodologies, including multi-step photolithographic and wet/dry etching steps. Furthermore, conventional photolithography can only reliably realize features/ L of $\sim 1 \mu\text{m}$, and while printing and laser cutting have simplified cOEET fabrication, it comes at the expense of performance. Moreover, to increase g_m , OEETs based on thick semiconducting films are typically employed, inevitably compromising the switching speed since high g_m values require efficient ion exchange between the electrolyte and the bulk semiconductor. Consequently, without progress in materials design, particularly for n-type semiconductors, and the realization of new device architectures, OEET applications will remain very limited in scope.

In a recent unpublished study, we demonstrated high-performance p- and n-type OEETs and complementary circuits by employing a vertical device architecture (hereafter named vOEET) easily fabricated by thermal evaporation/masking of impermeable and dense Au source/drain electrodes and spin-coating/photopatterning of the semiconductor channel (Figure. 48A). The key to this process is the use of

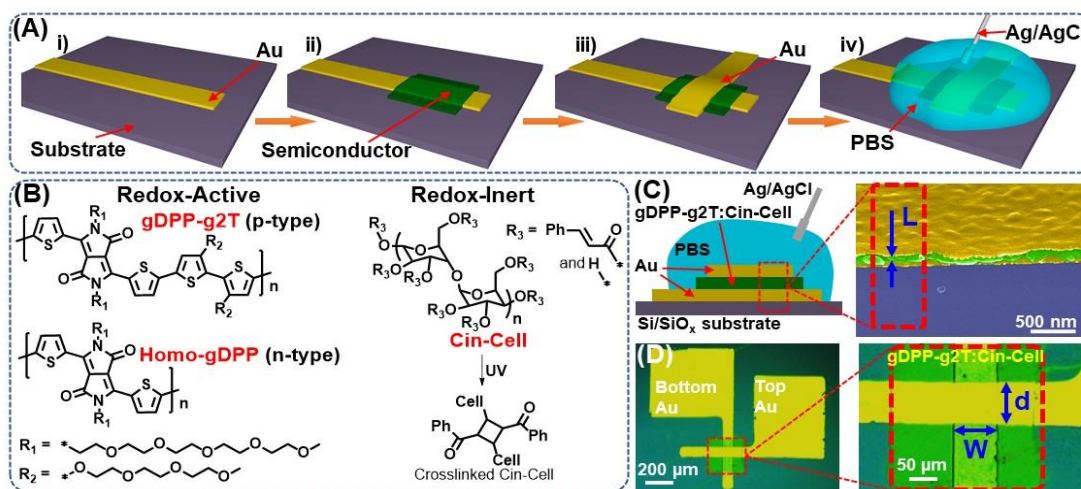


Figure. 48. Fabrication scheme and vOEET materials. (A) Fabrication of vOEETs: i). Thermal evaporation of bottom source electrode with a shadow mask; ii) Spin-coating/photopatterning of semiconducting layer; iii). Thermal evaporation of top drain electrode with a shadow mask; iv). Application of PBS electrolyte and Ag/AgCl gate electrode. (B) Chemical structures of the redox-active semiconducting polymers [gDPP-g2T (p-type); Homo-gDPP (n-type)], and redox-inactive crosslinkable polymer [Cin-Cell, crosslinking occurs via a photo-induced 2+2 cycloaddition reaction]. (C) Cross-section illustration a p-type vOEETs, along with a cross section SEM image (false colored) showing the semiconducting layer sandwiched between two dense Au electrodes ($W = L = 70 \mu\text{m}$). (D) Optical image of a p-type vOEET, where the electrode overlapping area is enlarged.

a redox-active [p-type (gDPP-g2T) or n-type (Homo-gDPP)] semiconductor blended with a redox-inert/photocurable polymer component [Cin-Cell] as the OECT channel (**Figure. 48B**). A vOECT geometry cross-section (**Figure. 48C**) and selected optical and SEM images (**Figure. 48D**) indicate that the channel length (L) is the semiconductor layer thickness (~ 100 nm), the widths of the bottom and the top electrodes define the channel width (W), and the nominal depth (d) of the semiconductor, respectively. Conventional OECTs (cOECTs) were also fabricated as controls.

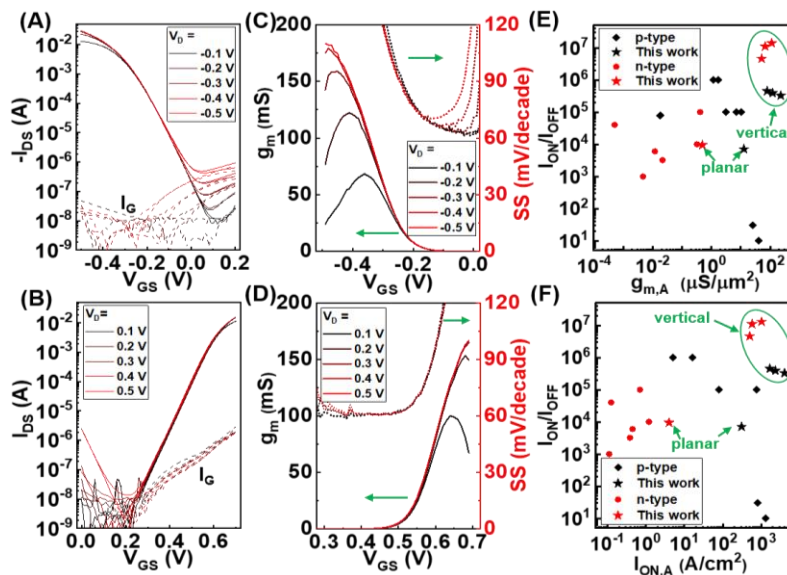


Figure. 49. OECT performance and comparison with literature data. (A, B) Representative transfer characteristics and (C, D) corresponding g_m and SS curves (A, C) of p-type gDPP-g2T ($W=d=30$ μm) and (B, D) n-type Homo-gDPP ($W=d=50$ μm) vOECTs. Comparisons of current on/off ratio ($I_{\text{ON}}/I_{\text{OFF}}$) versus (E) g_m per unit area ($g_{m,A}$) and (F) on-current per unit area ($I_{\text{ON},A}$) for different OECTs.

We tested vOECTs and cOECTs following standard procedures. The device transfer characteristics and the corresponding g_m /subthreshold swing (SS) plots (**Figs. 49A-D**) demonstrate extraordinary performance for both the p-type and n-type vOECTs, achieving maximum drain currents (I_{ONS}) of $8.2 \pm 0.5 \times 10^{-2}$ A ($V_D = -0.5$ V, $V_G = -0.5$ V) and $2.5 \pm 0.1 \times 10^{-2}$ A ($V_D = +0.5$ V, $V_G = +0.7$ V) and g_m s as high as 384.1 ± 17.8 mS and 251.2 ± 7.6 mS, respectively. Note that despite the ultra-small L (~ 100 μm), the $I_{\text{ON}}/I_{\text{OFF}}$ of both devices are impressive ($\geq 10^6$). All p- and n-type vOECTs retain stable turn-on voltages (V_{ON}) of $+0.10$ and $+0.21$ V as well as subthreshold swing (SS) of ~ 60 and ~ 62 mV/decade, respectively, upon scanning V_D from ± 0.1 to ± 0.5 V. More relevant parameters for vertical architectures are the area-normalized g_m ($g_{m,A}$) and I_{ON} ($I_{\text{ON},A}$). As shown in **Figs. 49E-F**, $g_{m,A}$ ($I_{\text{ON},A}$) as high as 226.1 $\mu\text{S}/\mu\text{m}^2$ (4036 A/cm 2) and 112.4 $\mu\text{S}/\mu\text{m}^2$ (1015 A/cm 2) are achieved for p- and n-type vOECTs, respectively. These values are about $18\times$ ($13\times$) and $100\times$ ($1000\times$) greater than those measured in the corresponding p- and n-type cOECTs, respectively. Thus, our p-type vOECTs exhibit the highest $g_{m,A}$ and $I_{\text{ON},A}$ values reported to date, even surpassing those of heavily doped/depletion mode PEDOT:PSS OECTs, while our n-type vOECT performance surpasses all of the previously reported OECTs (including p-type OECTs) in terms of $g_{m,A}$ and $I_{\text{ON}}/I_{\text{OFF}}$. Note that previously reported, vertical organic transistor architectures required either a permeable/ultra-thin (e.g., single-layer graphene) electrode or very complex photolithographic processes to accurately register the nanoscopic electrode/semiconductor layers for effective gate field modulation. The low SS of ~ 60 mV/decade measured for both vOECTs (Figure. 2C,D) is another convincing proof of the extremely effective gating

effect in this architecture. Furthermore, unlike cOECTs where the region with $SS \sim 60$ mV/decade, if achieved, is narrow, the present vOECTs have a very wide subthreshold region [0.0 ~ -0.2 V for gDPP-g2T and +0.3 ~ +0.6 V for Homo-gDPP] with SS near or equaling the ~ 60 mV/decade thermal limit. The wide subthreshold region is particularly useful for applications where high voltage gain and low power consumption are vital.

Cycling stability along with transient response of vOECTs were next assessed. As shown in **Figure. 50A-B**, for both p- and n-type vOECTs, >50000 stable switching cycles are recorded. Aside from the ultra-stable performance, vOECT turn-on transient time (τ_{ON}) is <1 ms for both devices (**Figure. 50C-D**), is $\sim 6-9\times$ shorter than those of the corresponding cOECTs ($\tau_{ON} = 6.75$ ms and 9.73 ms for p-type and n-type cOECTs).

To date, complementary logic has not been demonstrated for vertical organic transistors, due to immaturity of the fabrication processes and their inferior reliability. Here, vertically stacked complementary inverters (VSCIs) are possible due to the unique operation mechanism, simple fabrication process, and high stability of the present vOECTs.

Figure. 51A shows a schematic of the VSCI, where the n-type vOECT sits directly on top of p-type vOECT. Such 3D geometry enables much higher integration density as it requires 50% less footprint per inverter (**Figure. 51B**). The voltage output characteristics indicate that the VSCI possesses a sharp voltage transition with a gain up to ~ 150 (driving voltage = +0.7 V, **Figure. 51C**) and it is stable for >30000 switching cycles (**Figure. 51D**), further corroborating the excellent stability of both n-type and p-type vOECTs. Finally, a 5-stage ring oscillator was fabricated based on the VSCI (Figs. 4E and S25), and the output signal begins to oscillate between 0.0 and +0.7 V at a frequency of 17.7 Hz ($V_{DD} = +0.7$ V, **Figure. 51F**). This corresponds to a propagation delay of ~ 5.6 ms for each inverter.

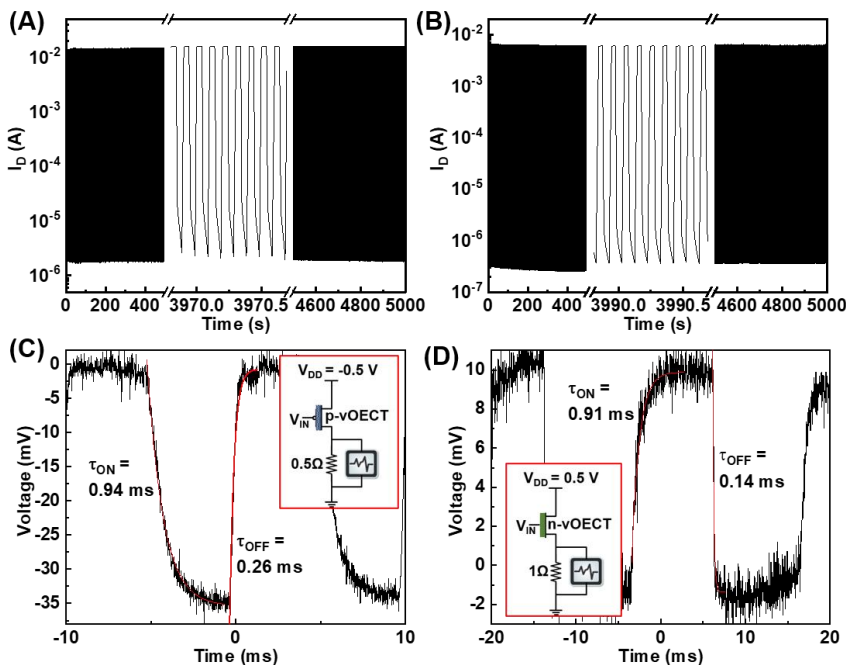


Figure. 50. vOECT stability and switching times. Cycling stability of (A) p-type gDPP-g2T and (B) n-type Homo-gDPP vOECTs, where $V_D = -0.1$ V, V_G is switching between 0 V and -0.7 V at a frequency of 10 Hz for the p-type vOECT, and $V_D = +0.1$ V, V_G is switching between 0 V and +0.7 V at a frequency of 10 Hz for n-type vOECT. Transient response of the p-type (C) and n-type (D) vOECTs, where transient behavior is monitored by the small voltage variation on a resistor through an oscilloscope (see insets of C and D). For both vOECTs $W = d = 30$ μm .

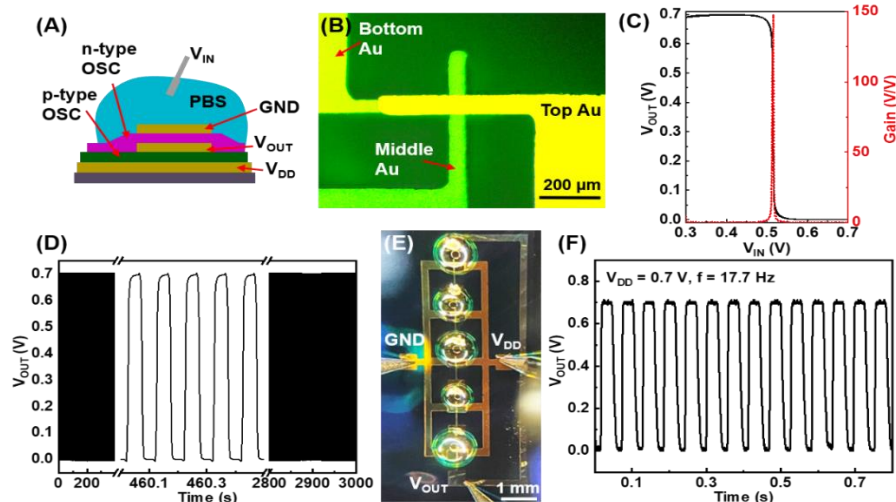


Figure. 51. Vertically stacked complementary circuits based on vOECTs (A) Illustration of a vertically stacked complementary inverter (VSCI) based on vOECTs. (B) Top view of the VSCI, where the Au electrode locations are indicated. (C) Voltage output characteristics of the VSCI, along with the voltage gain. (D) Switching stability of the VSCI with a switching frequency of 10 Hz. (E) Photograph of a 5-stage ring oscillator based on VSCI, and (F) Output characteristics of the oscillator.

In summary, the vOECT architecture demonstrated here, enabled by the synthesis of new polymers and engineering of the electro-active layer, is accessible by mature fabrication processes, exhibits high fidelity and stable performance characteristics, opening up possibilities for fundamentally new system designs in diverse applications, including wearables and implantable devices, where small effective footprint along with high g_m and low driving voltage are essential requirements. Moreover, vOECTs offer a new design paradigm for flexible and stretchable complementary devices and other relevant circuits.

See: Huang, W.; Chen, J.; Zheng, D.; Yao, Y.; Feng, L.-W.; Chen, Y.; Wang, Z.; Pankow, R.M.; Xia, Y.; Guo, X.; Cheng, Y.; Marks, T.J.; Facchetti, A. Vertical organic electrochemical transistors for complementary logic circuits, Under Revision